The Astrophysical Journal, 740:47 (17pp), 2011 October 10 doi:10.1088/0004-637X/740/1/47

STAR FORMATION RATES AND STELLAR MASSES OF Hα SELECTED STAR-FORMING GALAXIES AT $z = 0.84$: A QUANTIFICATION OF THE DOWNSIZING

Víctor Villar[1], Jesús Gallego[1], Pablo G. Pérez-González[1,4], Guillermo Barro[1], Jaime Zamorano[1], Kai Noeske[2], and David C. Koo[3]
[1] Departamento de Astrofísica, Facultad de CC. Físicas, Universidad Complutense de Madrid, E-28040 Madrid, Spain; vvillar@fis.ucm.es, j.gallego@fis.ucm.es, pgperez@fis.ucm.es, gbarro@fis.ucm.es, jzamorano@fis.ucm.es
[2] Space Telescope Science Institute, 3700 San Martin Drive, Baltimore, MD 21218, USA; noeske@stsci.edu
[3] Lick Observatory, University of California, Santa Cruz, CA 95064, USA; koo@ucolick.org
Received 2011 January 25; accepted 2011 July 20; published 2011 September 26

ABSTRACT

In this work we analyze the physical properties of a sample of 153 star-forming galaxies at $z \sim 0.84$, selected by their Hα flux with a narrowband filter. *B*-band luminosities of the objects are higher than those of local star-forming galaxies. Most of the galaxies are located in the blue cloud, though some objects are detected in the green valley and in the red sequence. After the extinction correction is applied, virtually all these red galaxies move to the blue sequence, unveiling their dusty nature. A check on the extinction law reveals that the typical extinction law for local starbursts is well suited for our sample but with $E(B-V)_{\rm stars} = 0.55\ E(B-V)_{\rm gas}$. We compare star formation rates (SFRs) measured with different tracers (Hα, far-ultraviolet, and infrared), finding that they agree within a factor of three after extinction correction. We find a correlation between the ratios $\rm SFR_{FUV}/SFR_{H\alpha}$, $\rm SFR_{IR}/SFR_{H\alpha}$, and the EW(Hα) (i.e., weighted age), which accounts for part of the scatter. We obtain stellar mass estimations by fitting templates to multi-wavelength photometry. The typical stellar mass of a galaxy within our sample is $\sim 10^{10}\ M_{\odot}$. The SFR is correlated with stellar mass and the specific SFR decreases with it, indicating that massive galaxies are less affected by star formation processes than less massive ones. This result is consistent with the *downsizing* scenario. To quantify this *downsizing* we estimated the *quenching* mass M_Q for our sample at $z \sim 0.84$, finding that it declines from $M_Q \sim 10^{12}\ M_{\odot}$ at $z \sim 0.84$ to $M_Q \sim 8 \times 10^{10}\ M_{\odot}$ at the local universe.

Key words: galaxies: evolution – galaxies: high-redshift

1. INTRODUCTION

During the last two decades, the cosmic star formation history of the universe has been widely studied in order to better constrain galaxy formation and evolution models. Large-area surveys and the use of larger telescopes have consolidated our knowledge at low-intermediate redshifts ($z = 0.0$–1.0; see Hopkins & Beacom 2006). Several measurements exist at higher redshifts (Pérez-González et al. 2005; Geach et al. 2008; Reddy & Steidel 2009; Hayes et al. 2010). At present we have started to probe the most distant universe at $z \sim 7$–8 (Bouwens et al. 2009, 2010).

In general, the star formation rate density (SFRd) history from the local universe to $z \sim 1$ is well accepted. Near $z \sim 1$, where the rise in SFRd from the local universe slows down, there are several measurements obtained through samples selected in a variety of ways and using different star formation rate (SFR) tracers. Results from Hα, UV, and IR agree reasonably, although with higher dispersion than at lower redshifts (Garn et al. 2010). This scattering originates (at least partially) from the two aforementioned processes: the sample selection and/or the SFR estimation. The estimations of the SFRd at this redshift have been measured mainly through UV (Lilly et al. 1996; Connolly et al. 1997; Cowie et al. 1999; Wilson et al. 2002; Schiminovich et al. 2005), IR (Flores et al. 1999; Le Floc'h et al. 2005; Pérez-González et al. 2005), and Hα (Glazebrook et al. 1999; Yan et al. 1999; Hopkins et al. 2000; Tresse et al. 2002; Doherty et al. 2006; Villar et al. 2008; Sobral et al. 2009; Ly et al. 2011). Therefore, it is important to constrain the potential differences that arise when one or another tracer is used to estimate SFRs.

Estimations of SFR through the UV flux are very sensitive to the extinction correction. UV detection also probes populations older than Hα, and is thus more sensitive to recent star formation history (Calzetti et al. 2005). The IR, on the other hand, is not affected by extinction but is very model dependent (Barro et al. 2011a, 2011b). Moreover, it is not well understood how the old population of stars contributes to the IR emission, but it could be a significant fraction (da Cunha et al. 2008; Salim et al. 2009). The Hα line is one of the best estimators as it is sensitive only to very young stars and is not affected by recent star formation history, which may still be detected by UV or IR. It has the problem that at $z > 0.5$ it moves to the near-infrared (NIR) domain, where large amounts of spectroscopy are still difficult to obtain, though several NIR multi-object spectrographs for 8–10 m class telescopes are coming in the next years. In addition, different methods have been used to measure the total Hα line flux, which could lead to discrepancies if some effects are not properly corrected. On one hand we have spectroscopy, long- or multi-slit or through fibers, where aperture corrections are needed to recover the total flux (see, for example, Doherty et al. 2006; Erb et al. 2006). On the other hand, we have the slitless spectroscopy (Yan et al. 1999; Hopkins et al. 2000) and narrowband (Villar et al. 2008; Sobral et al. 2009; Ly et al. 2011) techniques, which have the advantage that the total flux of the object is recovered and no aperture corrections are needed. Although correction from the nitrogen contribution is needed if the filter is not narrow enough, it is easier to estimate this effect than make aperture corrections. Obviously, the extinction is also important at this wavelength, though less so than in the UV.

[4] Associate Astronomer at Steward Observatory, The University of Arizona, 933 North Cherry Avenue, Tucson, AZ 85721, USA.

Thus, the Hα estimator is the best suited to study instantaneous star formation. As mentioned before, the problem is that at this redshift the line is observed in the NIR and little data to date are available. It is also interesting to assess if UV and IR provide SFRs comparable to those of Hα, given the large amount of data available today in these wavelengths.

The selection methods for the samples are also different and target different populations. Selecting the sample in the UV, for example, implies a bias against very obscured galaxies, which may not be detected unless very deep observations are carried out. On the other hand, the IR selected samples will favor the selection of objects with large amounts of dust, missing the blue and dust-free objects. Selections based in the Hα line will select the objects with ongoing star formation; thus, only star-forming galaxies (and active galactic nuclei [AGNs]) will be selected.

To study the population of galaxies that are actively forming stars, it is necessary to have a well-defined sample of star-forming galaxies. One of the best technique today is the use of narrowband filters targeting Hα.

A population of star-forming galaxies selected in this way is ideal for studying the SFR sequence, which refers to the correlation that exists between SFR and stellar mass. This correlation has been found at a wide range of redshifts, although evolution with respect to this parameter has been found (see Dutton et al. 2010 for a review). While the slope is almost constant, the SFR zero point increases from the local universe to redshift $z \sim 2$. From this redshift on, the trend remains almost constant with little evolution. There exists some discrepancy in the slope, which is somewhat lower than unity in all cases (see, for example, Noeske et al. 2007b; Elbaz et al. 2007; Salim et al. 2007).

However, some works do not find this correlation. Caputi et al. (2006) do not find any trend for their MIPS-selected sample at $z \sim 2$. More recently, Sobral et al. (2011) did not find any evidence of this sequence for their HiZELS sample at $z \sim 0.84$, selected with a narrowband filter targeting Hα.

This correlation implies that the slope of specific SFR (sSFR) versus mass is higher than −1. Obviously, if no correlation between stellar mass and SFR is found the slope of sSFR versus stellar mass is simply −1. The slope of this correlation is very important, as it tells us how the importance of star formation decreases over the already-formed stellar mass.

In this work we use a narrowband-selected sample of star-forming galaxies at $z \sim 0.84$, presented in Villar et al. (2008), to compare SFRs obtained from different tracers and to study the relation between stellar mass and SFR. The sample is very well suited for this study as (1) it is directly selected by star formation, so the population of star-forming galaxies is not biased and (2) the use of the narrowband filter technique provides reliable Hα SFRs to compare with FUV and IR estimations.

This paper is structured as follows: In Section 2, we present the sample and the available data sets. In Section 3, we describe the methods used to eliminate AGN contaminants. Absolute magnitudes and color are presented in Section 4. Section 5 presents a comparison of SFRs obtained through different estimators as well as a check on the extinction law more suited to our sample. Section 6 presents the stellar masses and their relation with SFR. Finally, we summarize our results and conclusions in Section 7.

Throughout this paper we use AB magnitudes. We adopt the cosmology $H_0 = 70\,\mathrm{km\,s^{-1}\,Mpc^1}$, $\Omega_m = 0.3$, and $\Omega_\lambda = 0.7$.

2. DATA

2.1. Sample

This paper analyzes an Hα selected sample of galaxies at $z = 0.84$. The objects are selected by their emission in the Hα+[N II] line and are thus selected due to intense star formation (except when activity at nuclei level is present). The sample was first described in Villar et al. (2008, hereafter V08), and the reader is referred to that paper for full details of the sample selection criteria. A brief summary of the process is presented here.

The sample was built using narrowband and broadband images in the J band of the near-infrared. The narrowband filter used in this work is J-continuum (J_C) centered at 1.20 μm, corresponding to Hα at $z = 0.84$. The search was performed using the near-infrared camera OMEGA-2000[5] of the 3.5 m telescope at the Calar Alto Spanish-German Astronomical Center (CAHA). OMEGA-2000 is equipped with a 2k × 2k Hawaii-2 detector with 18 μm pixels (0.″45 on the sky, 15′×15′ field of view). Three points were observed, two in the Extended Groth Strip (EGS) and another in the GOODS-North field, covering an area of ∼0.174 deg^2 and reaching 70% completeness at a line flux of $\sim 1.5 \times 10^{-16}$ erg s^{-1} cm^{-2}.

In a first step, 239 emission line candidates were selected (once excluded the stars) by their flux excess in the narrowband, showing a $J - J_C$ color excess significance $n_\sigma > 2.5$ in one or several apertures. Spectroscopic and photometric redshifts were then used to rule out contaminants, either emission line galaxies at other redshifts or objects selected by spectral features or noise. The sample was cross-checked against redshift catalogs on GOODS-N and EGS fields. A total of 76 objects were confirmed as genuine Hα emitters in the narrowband redshift range, 43 in the EGS and 33 in GOODS-N. Contaminants were mainly emission line galaxies at other redshifts, including a small sample of [O III] λλ4959,5007 emitters at $z \sim 1.4$ and a few objects not selected by line emission. The accuracy of selecting emission line galaxies was very high, around ∼90%. Spectroscopic redshifts were only available for 98 objects in the sample; therefore, photometric redshifts were used to get rid of interlopers for the rest of the sample. The quality of the estimated photometric redshifts was very high, with 86% of the objects in the whole EGS and 90% of the objects in GOODS-N (with reliable spectroscopic redshifts) within $\sigma_z/(1+z) < 0.1$. Considering the photometric redshifts, a total of 89 objects, 64 in the EGS and 25 in GOODS-N, were added to the final sample.

Since the original paper was published, new spectroscopic data have been made public, increasing the number of confirmed sources by 18 objects, for a total of 94. Only two objects were found to be incorrectly classified as Hα emitters and have been removed from the sample. Thus, the selection efficiency found in the original sample remains similar.

The final sample of Hα emitters at $z = 0.84$ contains 165 objects, 107 in the EGS and 58 in GOODS-N, 94 (57%) of them confirmed by optical spectroscopy (after including 3 objects with low-quality spectroscopic redshift). However, due to insufficient complementary data, we have discarded 12 objects. Hence, the sample used in this paper is composed of 153 objects.

Line fluxes have been recomputed using the formalism described in Pascual et al. (2007, hereafter P07), introducing the nitrogen contribution in the filters' effective widths. This forces us to assume an initial value for the nitrogen contribution, setting

[5] http://www.mpia-hd.mpg.de/IRCAM/O2000/index.html

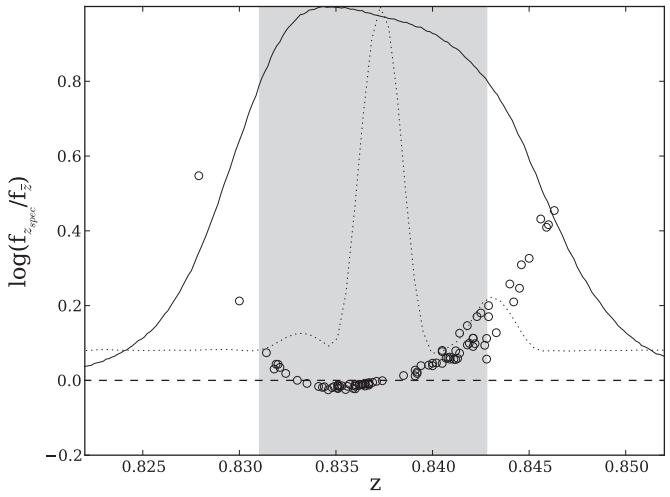

Figure 1. Line flux ratio between those computed with the individual spectroscopic redshift and with the average redshift. The narrowband filter shape is represented by the continuous line. The shaded region comprises the redshift range where the filter transmission is above 80%, where most of the objects are detected. The dotted line represents the Hα line surrounded by the nitrogen lines.

it to the average value found in V08: $I([\mathrm{N\,II}]\,\lambda6584)/\mathrm{I}(\mathrm{H}\alpha) = 0.26$. This provides an initial estimate of the Hα line flux without nitrogen contribution. With the equivalent width, we can estimate the nitrogen contribution, given the correlation between EW(Hα) and $I([\mathrm{N\,II}]\,\lambda6584)/\mathrm{I}(\mathrm{H}\alpha)$ found in the local Sloan Digital Sky Survey (SDSS) sample (see P07). We then re-estimate the nitrogen contribution and compute the line flux and equivalent width again. The latter provides a new estimation of the nitrogen contribution. The process is repeated until it converges, usually in two or three steps.

The line flux estimation through the narrowband and broad-band filters assumes a most likely redshift for the object, i.e., we assume a redshifted wavelength for the emission line based on the shape of the filter and on the cosmology (see Pascual et al. 2007). In fact, the objects distribute along the wavelength range covered by the narrowband filter and are most likely detected near the filter's central wavelength, where the transmission is high. Thus, assuming a most likely redshift for the objects seems reasonable for the majority of them. However, for the objects that are selected in the wings of the filter, where the transmission falls abruptly, the recovered fluxes differ significantly. Even in the regions of high transmission, there could be important effects due to the presence of the nitrogen lines. We can correct these effects by introducing the real redshift, which we know for half the sample, in the equations to compute the line flux (see Pascual et al. 2007).

In Figure 1, we compare the line fluxes estimated with the real redshift versus the ones estimated in the general way. The narrowband filter shape is also shown for reference. It can be seen that, for the objects that fall in the wings of the filter, the line flux is clearly subestimated. It is worth also noting that a significant line flux fraction is lost even when the transmission is high, as in the case of the objects with higher redshifts within the shaded region in the figure, where the transmission is always above 80%. This is due to the fact that the [N II] λ6584 line, which is the most intense of the two nitrogen lines, shifts to wavelengths where the transmission of the filter is greatly reduced; hence, if we do not take this effect into account, we over-correct the nitrogen contribution, estimating fainter line fluxes. The effect is also present at shorter wavelengths, though in that case the other nitrogen line ([N II] λ6548) is the one shifted to wavelengths with lower transmission. However, as this line is 3× weaker than the other one, the effect is less pronounced.

The amount of extinction for each galaxy was estimated through the FIR to UV flux ratio or the UV slope when the FIR data were not available (see V08). We used the extinction law derived by Calzetti et al. (2000). As new data are now available, especially regarding MIPS 24 μm, we have recomputed the extinctions for all the objects, considering, in addition, the results of the check on the extinction law (see Section 5.1). The median extinction for our sample is $1^{\mathrm{m}}.24$ in Hα, adopting values between 0^{m} and $3^{\mathrm{m}}.8$. Once these corrections are applied, Hα luminosities and SFRs are computed.

2.2. Additional Data

In order to estimate the different properties analyzed in this paper, we use several additional data sets sampling a wide range of the electromagnetic spectrum, from the far-ultraviolet (*GALEX* FUV) to the mid-infrared (MIPS 24 μm). These complementary data sets have been collected as part of the Universidad Complutense de Madrid (UCM) Rainbow database (see V08; Pérez-González et al. 2008; Barro et al. 2011a, for details) and have been gathered in part by the AEGIS (Davis et al. 2007) and GOODS (Dickinson & GOODS Legacy Team 2001) projects.

Briefly, in the EGS we have used optical data gathered with *MegaCam* at the 4 m Canada–France–Hawaii Telescope (CFHT), covering the following bands: u^*, g', r', i', and z'. We have also used B, R, and I images obtained with the same telescope but with the camera CFHT 12k, as described in Coil et al. (2004). Deep optical R-band data taken with SuprimeCam at Subaru 8 m as part of the Subaru SuprimeCam Weak-Lensing Survey (Miyazaki et al. 2007) are also available. In the domain of the near-infrared, images in the J band were obtained with Omega2000 as part of the data necessary to make the sample selection, and K-band images were obtained with Omega prime (Barro et al. 2009). Both instruments were located at the 3.5 m telescope at CAHA. Space-based optical images acquired with the Advanced Camera for Surveys (ACS) on board the *Hubble Space Telescope* (*HST*) are available in two bands: *F606W* and *F814W* (hereafter V_{606} and i_{814}). The *Galaxy Evolution Explorer* (*GALEX*; Martin et al. 2005) provides ultraviolet deep images in the far-ultraviolet (FUV; 153 nm) and the near-ultraviolet (NUV; 231 nm). The space observatory *Spitzer* observed the EGS field at 3.6, 4.5, 5.8, and 8 μm with the Infrared Array Camera (IRAC) instrument and in 24 μm with MIPS (Barmby et al. 2008).

In GOODS-N we made use of deep optical and near-infrared images (UBVRIzHK$_s$; Capak et al. 2004), as well as our own J- and K-band images, both of them obtained with Omega2000 (see V08 and Barro et al. 2009 for details). As in the case of the EGS, space-based observatories provide us with ultraviolet and infrared data, as well as high-resolution additional optical data. *GALEX* observed the region in far- and near-ultraviolet channels, while *Spitzer* observed the region in the mid-infrared (3.6–8 μm; IRAC) and in the far-infrared (24 μm; MIPS). The ACS on board *HST* contributed optical data in four bands *F435B* (B_{435}), *F606W* (V_{606}), *F775W* (i_{775}), and *F850LP* (z_{850}).

3. AGN CONTAMINANTS

The selection of a sample through the Hα line is susceptible to contamination by AGNs, as they are also powerful emitters in

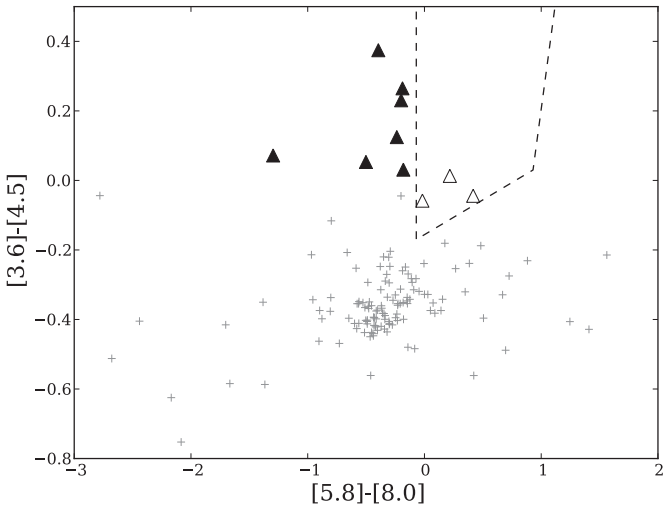

Figure 2. IRAC color–color plots for the selected sample with photometry in the four bands. The wedge delimited by the dashed polygon encloses the emitters powered by an AGN (open triangles). Seven objects (filled triangles) that fall outside this wedge, with positive [3.6]–[4.5] color, have also been considered AGNs because they have a rising SED, and the errors make them compatible with being located inside the wedge.

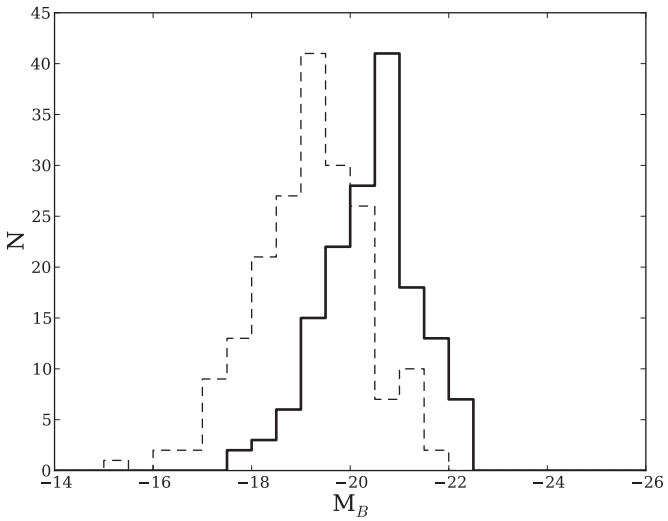

Figure 3. Histogram of rest-frame *B*-band absolute magnitudes. The thick line shows the distribution for the $z \sim 0.84$ sample. The dashed line corresponds to the UCM local sample, also selected by their Hα emission.

this line. Although both AGN and SFR could together contribute to the flux, disentangling both components is out of scope with the available data. Thus, we remove the objects classified as AGN from our sample.

In this work we detect the presence of 13 (8%) AGNs using two complementary methods: X-ray luminosity and mid-IR colors.

3.1. X-Ray Luminosity

We have cross-correlated our sample with the available X-ray catalogs in the EGS and GOODS-N fields. In the EGS fields we have the *AEGIS-X* X-ray catalog (Laird et al. 2009), which covers a large area within the EGS. Observations were made with the *Chandra* X-ray observatory with a nominal exposure time of 200 ks. In GOODS-N we have used the catalog created by Laird et al. from observations taken by *Chandra* with an exposure time of 2 Ms (Alexander et al. 2003). We find three X-ray counterparts in the EGS and four in GOODS-N within a 2″ search radius. The three objects in the EGS present high X-ray fluxes ($L_X > 6 \times 10^{42}$ erg s^{-1}), revealing their AGN nature. In GOODS-N, due to the depth of the observations, we find three objects whose X-ray luminosities are compatible with a star formation origin. The derived SFRs, using the calibration given by Ranalli et al. (2003), agree within a factor of three with the Hα derived ones. Thus, we have only discarded the four objects with X-ray luminosities whose origin could only be attributed to an AGN.

3.2. Mid-Infrared Colors

Some AGNs are heavily obscured, and even the deepest X-ray observations can miss a significant fraction of them (Park et al. 2010). In this case, X-ray emission is absorbed by the circumnuclear dust and re-emitted in the infrared. One way to detect these obscured AGNs is by looking at their mid-IR colors. The color criterion defined by Stern et al. (2005) is based on differences in the mid-IR emission shown by star-forming galaxies and AGNs. The spectral energy distribution (SED) of star-forming galaxies peaks at 1.6 μm, falling at longer wavelengths (Garn et al. 2010). In the case of an AGN, the emission does not decrease at longer wavelengths due to the re-emission of light absorbed by the circumnuclear region in the mid-IR. Unfortunately, the distinction becomes less pronounced at our redshift, as pointed out by Stern et al. (2005).

In Figure 2 we show the objects that fulfill the criterion (inside the dashed polygon), which are AGNs, as well as the rest of the objects, which are pure star-forming galaxies. A total of three galaxies fall within the wedge defined by Stern et al. Seven other objects with positive [3.6]–[4.5] color fall relatively close to this wedge (except one), although they do not fulfill the criterion. We have decided to consider these objects as AGN contaminants, given that photometry errors could have placed them outside the region and that they have a rising SED ([3.6]–[4.5]>0). Only one of these ten objects has an X-ray counterpart.

We note that this classification could be selecting star-forming galaxies instead of AGNs, as pointed out by Donley et al. (2008). We decide to exclude them all to make sure we are not introducing any AGNs.

Another way to check the presence of obscured AGNs is through the power-law criterion (Alonso-Herrero et al. 2006). We do not find any galaxy showing this characteristic power-law shape in the mid-IR SED.

4. PHOTOMETRIC PROPERTIES

The histogram of rest-frame *B*-band magnitudes for our sample is shown in Figure 3. The median of the distribution is $M_B = -20\overset{m}{.}5$, reaching the most luminous objects $M_B = -22\overset{m}{.}5$. The standard deviation of the distribution is $0\overset{m}{.}9$. For comparison we also show in the figure the UCM local sample of star-forming galaxies (Zamorano et al. 1994, 1996) also selected by the Hα line flux. In the local sample no galaxies brighter than $M_B \sim -22$ are detected, suggesting that star-forming galaxies at $z \sim 0.84$ are more luminous than their local analogous galaxies. The volume sample in each survey is very different: 10^5 Mpc^3 for the typical object in the UCM, while for our sample the surveyed volume is $\sim 15 \times 10^3$ Mpc^3. However, given the larger volume explored in the UCM survey with respect to our survey, it is clear that star-forming galaxies at $z \sim 0.84$ are in general brighter in the *B* band.

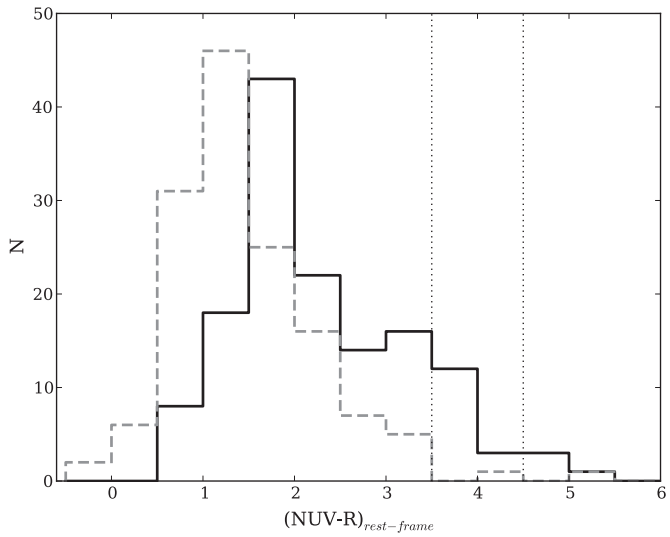

Figure 4. Histogram of rest-frame NUV−R colors for our sample. The black line represents the sample without applying the correction for extinction. The dashed line shows the distribution once the extinction has been corrected. It can be seen that most objects fall in the blue cloud (NUV − R < 3.5). Before the extinction correction is applied, some objects fall in the green valley (3.5 < NUV − R < 4.5) and in the red sequence (NUV − R > 4.5). After it is applied, only two objects remain outside the blue cloud.

A clear bimodality in the color of galaxies was first found by Strateva et al. (2001) by analyzing the optical colors of the SDSS sample. Galaxies divide mainly in two groups: the blue cloud and the red sequence. The blue cloud is populated by star-forming galaxies, whereas galaxies with no recent star formation fill the red sequence. This bimodality is also present at higher redshifts (Willmer et al. 2006; Faber et al. 2007). An intermediate region, the green valley, was identified using the NUV − R color (Wyder et al. 2007). The galaxies within this group are either in a transition phase from the blue cloud to the red sequence, due to the shutdown of star formation, or are star-forming galaxies with high extinction (Martin et al. 2007; Salim et al. 2007). In Figure 4, we depict the NUV − R color for our sample. Most of the sample belongs to the blue cloud (NUV − R < 3.5), in agreement with their star-forming nature. However, some galaxies fall in the green valley (3.5 < NUV − R < 4.5) and a few of them in the red sequence (NUV − R > 4.5). This can be explained by the high extinction present in these galaxies, and, indeed, when the extinction is corrected only two galaxies fall outside the blue cloud. One of them is not confirmed by optical spectroscopy, so it might not be a real $z \sim 0.84$ emitter. In fact, its photo-z χ^2 distribution does not present a clear peak at that redshift but rather a flatter distribution. The other one, although confirmed by optical spectroscopy, is very close to another galaxy (<2″), and its photometry might be affected.

5. STAR FORMATION RATES

This work uses Hα luminosity as the principal estimator of the instantaneous SFR of galaxies. The Hα line flux has been used to select the sample, making it very suitable for studying star formation processes, as it has been selected by this property. However, star formation involves physical processes whose imprint becomes observable along a wide range of the electromagnetic spectrum: X-rays, ultraviolet, forbidden recombination lines ([O II] λ3727), far-infrared, radio, etc. In this work, in addition to Hα, given the depth and coverage of the multi-wavelength data available, we estimate SFRs through far-ultraviolet and far-infrared luminosities. Each tracer is affected by different phenomena and originates from different physical mechanisms, related (at least in part) to star formation processes. Thus, the different results obtained with different tracers could yield some information about the properties of the galaxy that hosts the star formation processes.

The Hα line is produced due to the recombination processes in ionized hydrogen present in the clouds of gas and dust that surround the newly formed stars. The massive type O and B stars produce an intense radiation field capable of ionizing the hydrogen atoms. When equilibrium is reached, the recombination of the free electrons with the ionized hydrogen produces several emission lines, the Hα line being one of the most luminous in the visible. To obtain the SFR from the Hα luminosity (L_{H_α}), we apply the relation given by (Kennicutt 1998):

$$\mathrm{SFR}_{\mathrm{H}\alpha}(M_\odot\ \mathrm{yr}^{-1}) = 7.9 \times 10^{-42} L_{\mathrm{H}_\alpha}(\mathrm{erg\ s}^{-1}), \quad (1)$$

where a Salpeter (1955) initial mass function (IMF) has been considered. Hα directly traces the SFR and has very low dependence on metallicity or on ionization conditions of the gas cloud. Among the adverse effects, the most important are the extinction and the escape fraction of ionizing photons. The former is common to optical indicators, and extinctions as high as ∼4 mag in the Hα line can be found in our sample, although the median extinction is 1.24 mag. The latter implies a subestimation of the SFR if the escape fraction is high. Fractions up to 50% have been measured for individual H II regions (Oey & Kennicutt 1997). However, this fraction turns out to be much lower when the whole galaxy is considered (which is our case), decreasing to less than 3% as measured by Leitherer et al. (1995). Another adverse effect recently shown by Lee et al. (2009) is the underestimation of SFR for dwarf galaxies. Nevertheless, this effect appears for SFRs below 0.03 $M_\odot$ yr^{-1}, two orders of magnitude lower than our lowest SFR, so it does not affect the estimations for our samples.

Ultraviolet emission comes directly from young massive stars formed in the star formation region. To compute the UV SFRs we use the following calibration (Kennicutt 1998):

$$\mathrm{SFR}_{\mathrm{FUV}}(M_\odot\ \mathrm{yr}^{-1}) = 1.4 \times 10^{-28} L_{\mathrm{FUV}}(\mathrm{erg\ s}^{-1}\mathrm{Hz}^{-1}), \quad (2)$$

where L_{FUV} is the FUV luminosity spectral density. Although we apply it to the UV flux in 1500 Å, the calibration is valid in the 1500–2800 Å range, as the spectrum is nearly flat in that regime.

The dust in a galaxy absorbs part of the radiation emitted at short wavelengths and re-emits it in the IR. This absorption is more intense at shorter wavelengths. Given that young stars radiate most of their luminosity in the ultraviolet, there exists a correlation between IR luminosity and star formation. The correlation between luminous regions in Hα and in IR confirm the validity of the latter as a valid star formation tracer (see Devereux et al. 1997 for details). More recently, observations carried out with the *Spitzer Space Telescope*, with improved resolution, confirmed those results (Calzetti et al. 2005; Pérez-González et al. 2006).

The calibration of the infrared emission as a star formation tracer is not simple, as it depends on several factors: geometrical distribution and optical thickness of the dust, fraction of emission coming from old stars, etc. In an ideal case, the star-forming regions would be surrounded by dust clouds, opaque enough to

re-radiate the entire region's luminosity. However, these ideal conditions differ from the actual scenario, due in part to the aforementioned factors. This complicates the calibration and increases the dispersion.

Given the infrared luminosity $L_{\rm IR}$(8–1000 μm), the following relation can be used to estimate the SFR (Kennicutt 1998):

$$\mathrm{SFR_{IR}}(M_\odot \mathrm{yr}^{-1}) = 1.71 \times 10^{10} L_{\rm IR}(L_\odot), \quad (3)$$

where $L_{\rm IR}$ corresponds to the total infrared luminosity between 8 and 1000 μm.

The great advantage of this tracer is that it is not affected by extinction. However, the estimations are sensitive to other factors such as the dust spatial distribution, old stellar population contribution, etc. Moreover, it is necessary to estimate the total infrared luminosity in the range 8–1000 μm. In general, this is done with a few measurements in the infrared, usually with wavelengths shorter than 24 μm. Recent works have demonstrated that a better relation exists between Hα and flux at 24 μm (see, for example, Pérez-González et al. 2006; Calzetti et al. 2007; Rieke et al. 2009; Kennicutt et al. 2009). However, this wavelength is not available for our $z = 0.84$ sample because the MIPS observed 24 μm data turn into rest frame ~13 μm.

5.1. Dust Attenuation

In order to properly compare the SFRs it is necessary to correct the effect introduced by extinction. In V08 we computed the extinction using the dust flux to UV flux ratio and the UV slope when the IR data were not available. This provided us with the attenuation in the FUV band, from which the attenuation at the Hα line was estimated assuming a Calzetti et al. (2000) extinction law, given the star-forming nature of our sample. This law considers that the nebular emission is more extinct than the stellar emission: $E(B-V)_{\rm stars} = \gamma\, E(B-V)_{\rm gas}$, with $\gamma = 0.44$. However, this factor may be different for different populations and/or dust geometry and may depend on redshift. Garn et al. (2010) found for the S09 sample that $\gamma \sim 0.5$, slightly higher than the typical value. Erb et al. (2006) found that, in order to reconcile their SFR estimations in the UV and Hα for their $z \sim 2$ UV selected sample, the same color excess has to be affecting both the gas and stars, i.e., $\gamma \sim 1$. Yoshikawa et al. (2010), using a sample of *BzK* selected galaxies at $z \sim 2$, found that their data were consistent with the original $\gamma = 0.44$ value, although galaxies with low SFRs are consistent with $\gamma = 1$.

The γ factor arises from the fact that the UV and the nebular emission have different spatial origins due to the different population of stars each one is tracing. Whereas the nebular emission originates from very massive and young stars, the UV emission originates from less massive and older stars. Thus, this factor might be different depending on the star formation history of the galaxies. Moreover, the extinction law may be different from that of Calzetti et al. (2000). Thus, it is important to estimate this value for our sample and, if possible, to verify the suitability of the Calzetti et al. extinction law (with the same or different γ) for our sample.

We tackle this problem by estimating the extinction law in the UV regime and in the Hα line. Thanks to the large amount of optical broadband data available, we can obtain several estimations of the SFR (affected by extinction) at different wavelengths within the UV, in addition to the Hα estimation. If we assume that every different SFR estimation, once corrected for extinction, gives the same SFR, we can obtain the extinction in each wavelength and compare it to the total SFR:

$$\mathrm{SFR^{total}} = \mathrm{SFR^{uncor}_{UV_n}} 10^{0.4\,\kappa(\mathrm{UV_n})\,\mathrm{E(B-V)_{stars}}} \quad (4)$$

$$\mathrm{SFR^{total}} = \mathrm{SFR^{uncor}_{H\alpha}} 10^{0.4\,\kappa(\mathrm{H\alpha})\,\mathrm{E(B-V)_{gas}}}, \quad (5)$$

where $\mathrm{SFR^{total}}$ is the SFR given by IR(8–1000 μm) and UV_n represents each different UV wavelength. Thus, we can obtain $\kappa(\lambda)$ for different wavelengths as follows:

$$\kappa(\mathrm{UV}_n) = \frac{2.5}{E(B-V)_{\rm stars}} \log\left(\frac{\mathrm{SFR^{total}}}{\mathrm{SFR^{uncor}_{UV_n}}}\right) \quad (6)$$

$$= \frac{2.5}{\gamma\, E(B-V)_{\rm gas}} \log\left(\frac{\mathrm{SFR^{total}}}{\mathrm{SFR^{uncor}_{UV_n}}}\right) \quad (7)$$

$$\kappa(\mathrm{H\alpha}) = \frac{2.5}{E(B-V)_{\rm gas}} \log\left(\frac{\mathrm{SFR^{total}}}{\mathrm{SFR^{uncor}_{H\alpha}}}\right), \quad (8)$$

where we have everything related to the color excess in the gas $E(B-V)_{\rm gas}$ through the γ factor. At this point, we are interested in the shape of the extinction law and it is therefore necessary to get rid of the amount of extinction, parameterized by $E(B-V)_{\rm gas}$ for each galaxy. We normalize then by the value at 6563 Å:

$$\kappa_{6563}(\mathrm{UV}_n) = \frac{1}{\gamma} \frac{\log\left(\frac{\mathrm{SFR^{total}}}{\mathrm{SFR^{uncor}_{UV_n}}}\right)}{\log\left(\frac{\mathrm{SFR^{total}}}{\mathrm{SFR^{uncor}_{H\alpha}}}\right)} \quad (9)$$

$$\kappa_{6563}(\mathrm{H\alpha}) = 1, \quad (10)$$

where γ is not known. Therefore, we can only measure $\gamma \cdot \kappa(\mathrm{UV}_n)$ empirically. If we fit these values to an extinction law we can obtain this factor, which was our original goal.

In our sample there are data available for four bands in the UV rest frame within the range 1900–3000 Å, where the spectrum is almost flat once the dust effect has been removed and we can use the Kennicutt (1998) calibration. In both EGS and GOODS-N there are observations at ~1950 Å and ~2400 Å. There exists an additional third band in each field, but with different wavelengths: ~2650 Å in EGS and ~2950 Å in GOODS-N. Thus, we sample four different wavelengths in the UV. There are 72 objects for which all the UV and IR needed data are available.

There are two things we want to check: (1) which γ factor is appropriate for our sample, and (2) is the Calzetti et al. extinction law suitable for our sample? To answer these questions, we fit two different extinction laws to the data: the aforementioned Calzetti et al. extinction law and the Cardelli et al. (1989) law. The fitting process gives us the γ factor needed to make the UV and Hα measurements consistent, and it also allows us to check which extinction law provides better agreement with the data, through the computation of the χ^2 value of each fit.

In Figure 5, we show the $\gamma \cdot \kappa(\mathrm{UV}_n)$ obtained by computing the median of the different UV measurements. We also show the Calzetti and Cardelli extinction laws that best fit the data points. The Calzetti extinction law is more consistent with our measurements. We obtain the following χ^2 values for each

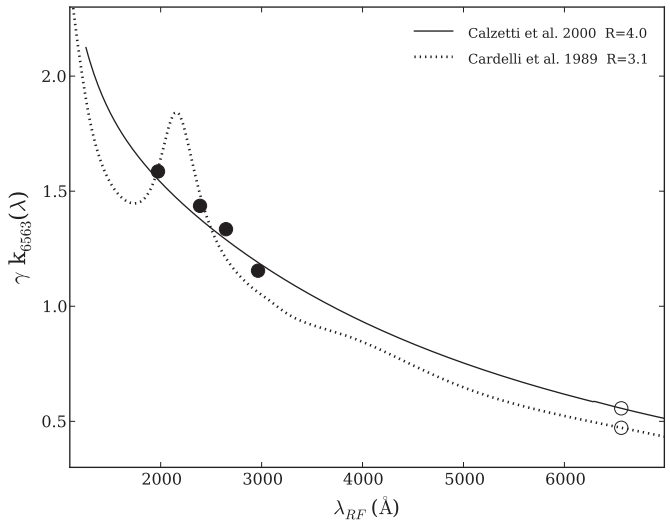

Figure 5. Derived reddening curve for our sample (filled circles). The continuous line represents the Calzetti extinction law with $\gamma = 0.55$. The dotted line corresponds to the Cardelli extinction law with $\gamma = 0.46$. The open circles represent the reddening that would have the stellar continuum for each extinction law and their corresponding γ values.

Table 1
Comparison Between Total and Confirmed Samples

Property (1)	Total Sample (2)	Confirmed Sample (3)
γ Calzetti et al. (2000)	0.55	0.56
$\langle SFR_{H\alpha} \rangle$	$11^{+22}_{-7}\ M_\odot\ yr^{-1}$	$14^{+23}_{-9}\ M_\odot\ yr^{-1}$
$\langle SFR_{FUV}/SFR_{H\alpha} \rangle$	0.89	0.87
$\langle SFR_{IR}/SFR_{H\alpha} \rangle$	0.95	0.96
log ($M_Q/M_\odot$)	12.0 ± 0.2	12.2 ± 0.2

Note. Column 1: measured property; Column 2: value obtained using the whole sample; Column 3: value obtained using the sample confirmed with optical spectroscopy.

fit: $\chi^2_{Cal00} = 0.2$ versus $\chi^2_{Car89} = 0.6$. These values are below one due to the large errors with which we are working. We consider that the Calzetti et al. law is best suited for our sample, as the residuals are lower and we are dealing with the same uncertainties. In both cases a heavier attenuation in the nebular gas than in the stellar continuum is needed, i.e., a γ factor lower than one. We obtain $\gamma_{Cal00} = 0.55 \pm 0.20$ and $\gamma_{Car89} = 0.46 \pm 0.17$. If we do the analysis on a galaxy-by-galaxy basis we obtain similar results. The extinction analysis on individual galaxies and the relation with other properties will be presented in a future paper.

If we repeat this process discarding all objects not confirmed by spectroscopy, we obtain very similar results. In this case, the number of galaxies is reduced to 57 and we obtain $\gamma_{Cal00} = 0.56 \pm 0.20$ and $\gamma_{Car89} = 0.47 \pm 0.17$. The χ^2 values for each fit are now $\chi^2_{Cal00} = 0.4$ versus $\chi^2_{Car89} = 1.4$. A comparison among results (from this and other sections) for the whole sample and that containing only spectroscopically confirmed objects is shown in Table 1.

To summarize, the Calzetti et al. extinction law is well suited for our sample with $\gamma = 0.55$, a value slightly higher than the original 0.44 value. We have assumed this extinction law with this γ factor on the dust attenuation estimations.

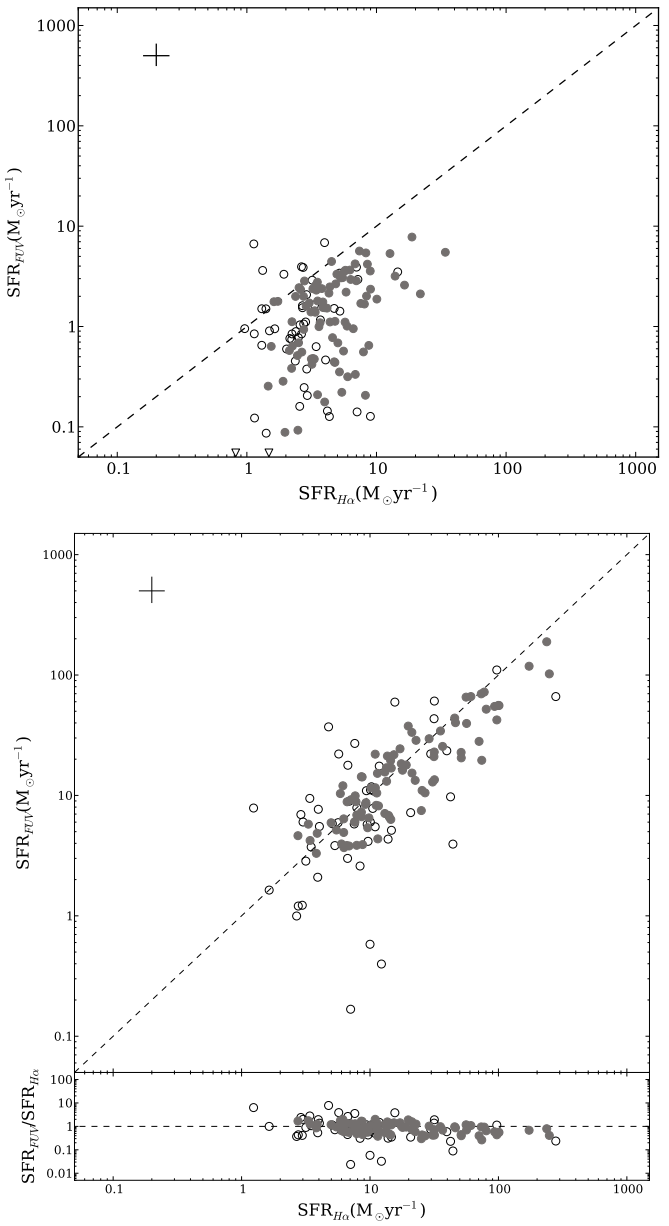

Figure 6. Comparison of SFRs inferred from Hα luminosity and FUV luminosity. Top: no extinction correction applied. Bottom: extinction correction applied to both tracers. Filled circles are objects confirmed by optical spectroscopy, whereas open circles are objects without spectroscopic confirmation. We also show the $SFR_{FUV}/SFR_{H\alpha}$ ratio vs. $SFR_{H\alpha}$.

5.2. Comparison of SFR Tracers

5.2.1. Ultraviolet

In this section, we compare the FUV-derived SFR with that coming from the Hα luminosity. The reader should note that in this section we use the FUV luminosity (1500 Å), which has not been used in the computation of γ in the previous subsection, thus assuring the independence of the results.

The comparison between Hα and FUV SFRs is plotted in Figure 6. The top panel shows SFRs estimated without extinction corrections. Objects confirmed by optical spectroscopy are shown as filled circles, whereas the objects lacking spectroscopic confirmation are shown as empty circles. The effect of the reddening is clearly visible as FUV SFRs are, in general, lower than those obtained through Hα. The median value

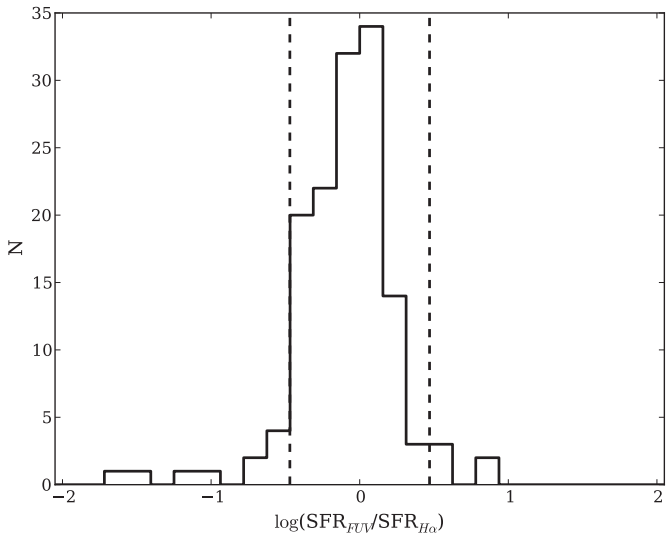

Figure 7. Histogram of the ratio $SFR_{FUV}/SFR_{H\alpha}$ in logarithmic scale. Most of the objects concentrate around the unity ratio. There are also wings on both sides of the distribution, with some extreme cases in which SFR is subestimated up to 10–100. The tail of objects for which the UV subestimates the SFR is more extended than in the case of the Hα. The dashed lines enclose the objects whose SFRs agree within a factor of three.

and standard deviation for the FUV estimates are $\langle SFR_{FUV}\rangle = 1.5^{+3.3}_{-0.9}\ M_\odot\ yr^{-1}$, while for the H$\alpha$ line we find $\langle SFR_{H\alpha}\rangle = 3.5^{+3.2}_{-1.7}\ M_\odot\ yr^{-1}$. Objects not confirmed by spectroscopy show a higher dispersion, although it is compatible with that of the confirmed objects once a few outliers are removed.

In the bottom panel of Figure 6, we show the effect of applying the extinction corrections. The SFR range has a considerable span, going from 2–10 $M_\odot\ yr^{-1}$ when the effect of extinction is not corrected to 2–300 $M_\odot\ yr^{-1}$ when it is corrected. Estimations coming from both tracers now agree within a factor of three. The statistical values are in this case $\langle SFR_{FUV}\rangle = 10^{+21}_{-7}\ M_\odot\ yr^{-1}$ and $\langle SFR_{H\alpha}\rangle = 11^{+22}_{-7}\ M_\odot\ yr^{-1}$. The good agreement corroborates the fact that our extinction corrections are working well and that these galaxies do not host star-forming regions totally attenuated in the UV but visible in Hα, at least globally. There still can be regions totally obscured both in UV and in the optical, which will only arise in IR observations. We will explore this possibility in Section 5.2.2.

To explore in more detail the differences between both tracers, we study the $SFR_{FUV}/SFR_{H\alpha}$ ratio for each object. The median value is $\langle SFR_{FUV}/SFR_{H\alpha}\rangle = 0.89$, which tells us that the Hα line yields slightly higher values than the FUV for the SFR, although they are compatible considering the errors. As we use the FUV luminosity, which has not been used in the computation of γ, it is possible to have ratios below or above one. As the FUV is at a shorter wavelength, the higher extinction could totally attenuate more regions than at higher wavelengths, thus underestimating the SFR. If we use SFRs obtained from 2800 Å instead, the ratio $SFR_{2800}/SFR_{H\alpha}$ becomes one, as this wavelength is in the regime used in the extinction law check. The number of objects is also different, as objects used in the extinction section must have IR data. The distribution of ratios is shown in Figure 7. Although the agreement is quite good, with 90% of the objects within a factor of three, there are objects whose SFR is overestimated by Hα, with a few in the opposite case. If we consider only our spectroscopically confirmed sample, we find almost the same results: $\langle SFR_{H\alpha}\rangle = 14^{+23}_{-9}\ M_\odot\ yr^{-1}$ and $\langle SFR_{FUV}/SFR_{H\alpha}\rangle = 0.87$.

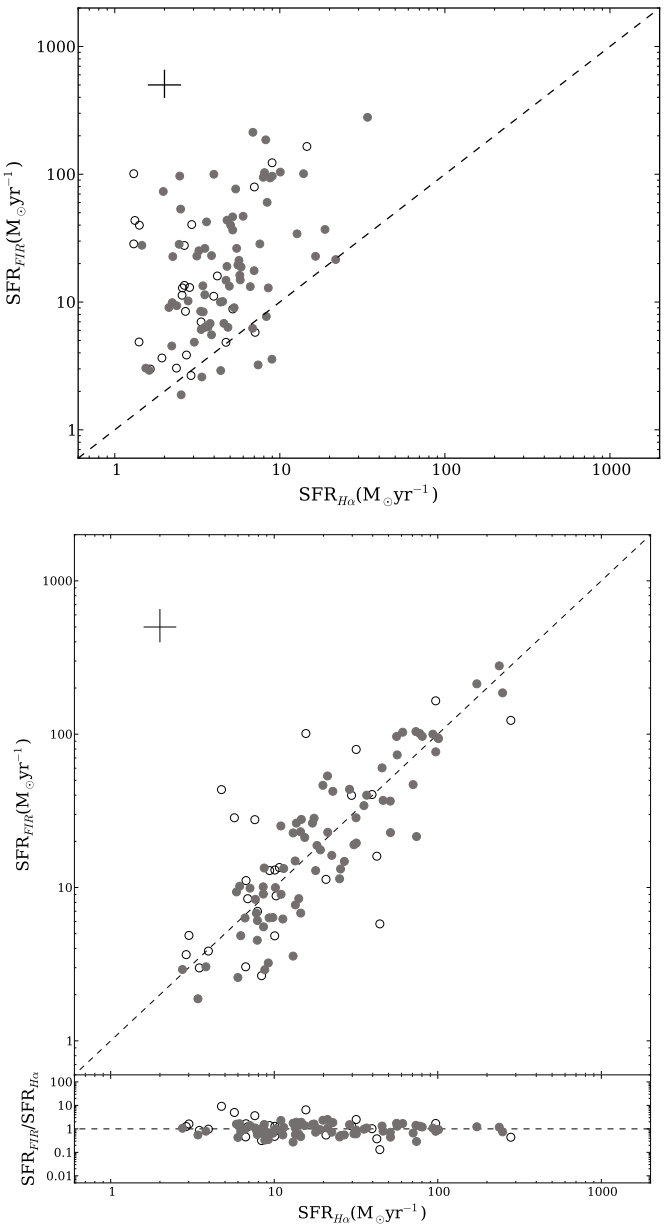

Figure 8. Comparison of SFRs inferred from Hα luminosity and IR luminosity. Top: no extinction correction applied. Bottom: extinction correction applied to Hα. Filled circles are objects confirmed by optical spectroscopy, whereas open circles are objects without spectroscopic confirmation. We also show the $SFR_{IR}/SFR_{H\alpha}$ ratio vs. $SFR_{H\alpha}$.

The general agreement between both tracers is also found in the local universe (Salim et al. 2007). At $z \sim 2$, Erb et al. (2006) also compared these tracers to a sample of Lyman-break galaxies (Steidel et al. 1996, 1999) selected through the U_nGR criterion (Adelberger et al. 2004; Steidel et al. 2004). Their result shows good agreement between both tracers, with a dispersion similar to that of our sample. At that same redshift, Yoshikawa et al. (2010) find that both tracers are roughly consistent, although SFRs measured with Hα are systematically larger by 0.3 dex.

5.2.2. *Infrared*

It is very interesting to check infrared SFRs to determine whether Hα is losing substantial star formation due to dust attenuation. The top panel of Figure 8 shows the comparison between both tracers before applying any extinction correction.

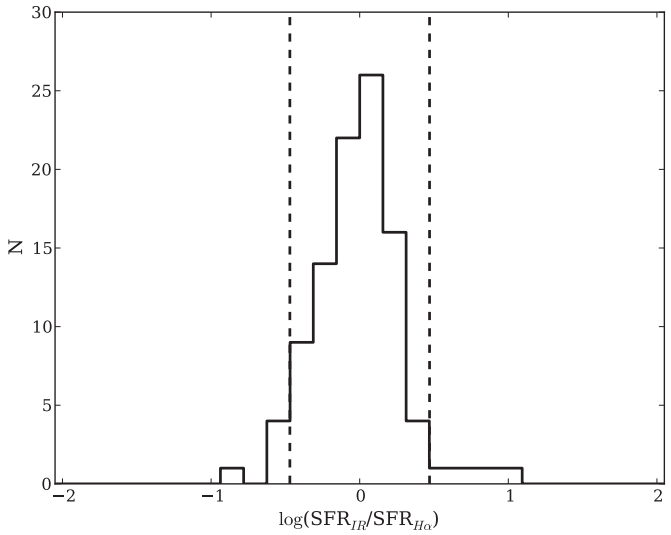

Figure 9. Histogram of the ratio $SFR_{IR}/SFR_{H\alpha}$ in logarithmic scale. Most of the objects concentrate around the unity ratio, though in general the IR estimates are higher than those obtained with Hα. The dashed lines enclose the objects whose SFRs agree within a factor of three.

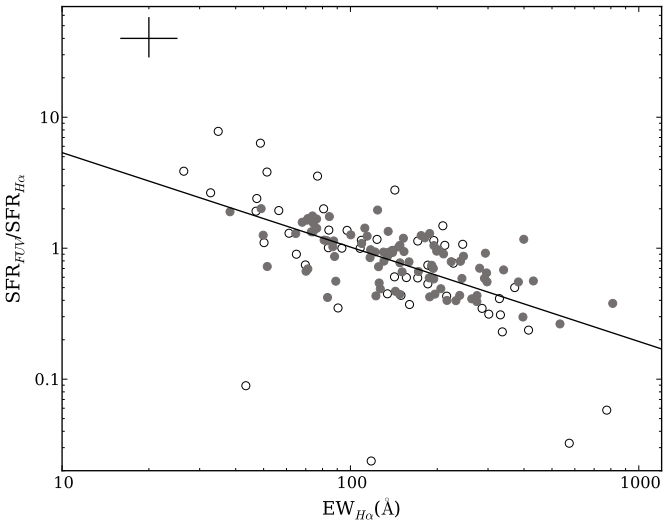

Figure 10. $SFR_{FUV}/SFR_{H\alpha}$ ratio vs. EW(Hα). The line is the best linear fit to the data in logarithmic scale. The high EW(Hα) objects tend to have lower $SFR_{FUV}/SFR_{H\alpha}$ ratios, whereas the lower EW(Hα) objects tend to have higher ratios.

Not surprisingly, Hα systematically subestimates the SFR. There is a large scattering, which reflects the different attenuations that each galaxy suffers. It is worth noting that we only have infrared luminosities for the fraction of the sample detected with MIPS (100/140, 71%). The IR limiting flux for a completeness of 80% is 83 μJy in our surveyed fields, which translates into $\sim 10\, M_\odot\, \mathrm{yr}^{-1}$ for our redshift.

The median and standard deviation is $\langle SFR_{H\alpha}\rangle = 4.1^{+3.7}_{-1.9}\, M_\odot\, \mathrm{yr}^{-1}$ for Hα, while for the IR we obtain $\langle SFR_{IR}\rangle = 15^{+34}_{-11}\, M_\odot\, \mathrm{yr}^{-1}$. As in the case of UV, we do not observe systematic differences between spectroscopically confirmed and unconfirmed objects.

Once the extinction corrections are applied (see the bottom panel of Figure 8), we find $\langle SFR_{H\alpha}\rangle = 15^{+29}_{-10}\, M_\odot\, \mathrm{yr}^{-1}$, which agrees very well with the IR-derived value. If we work with the ratios of SFRs, we find that Hα provides slightly higher estimates ($\langle SFR_{IR}/SFR_{H\alpha}\rangle = 0.95$) in agreement with IR estimates within uncertainties. In Figure 9 we show the $SFR_{IR}/SFR_{H\alpha}$ distribution. In the figure it can be seen that Hα estimates are systematically higher than the IR estimates. However, for 91% of the objects, the SFRs agree within a factor of three. If we consider only our spectroscopically confirmed sample we find very similar results (see Table 1): $\langle SFR_{H\alpha}\rangle = 17^{+30}_{-10}\, M_\odot\, \mathrm{yr}^{-1}$ and $\langle SFR_{IR}/SFR_{H\alpha}\rangle = 0.96$.

5.3. Exploring the Scatter

It is interesting to explore the reasons why discrepancies originate between different tracers. The Hα line is only produced when the star-forming region includes stars with masses above $10\, M_\odot$. Thus, only star-forming regions aged less than 20 Myr are detectable through this line, since older regions would not have stars massive enough to photoionize the surrounding gas. There are other factors that could affect this, such as metallicity, the fraction of ionizing photons that escape, etc. This set of conditions does not hold for the other tracers, which have their own factors. Ultraviolet, for example, is more sensitive to less massive stars, being more affected by the star formation history of the galaxy. Infrared is also affected by the star formation history, as evolved stars can make a significant fraction of the infrared emission (da Cunha et al. 2008). Kennicutt et al. (2009) find that 50% of the infrared emission in the local galaxies within the SINGS sample comes from evolved stars. At higher redshifts, Salim et al. (2009) find for a sample with $z < 1.4$ and with star formation ($NUV - R < 3.5$) that the infrared flux fraction originating from intermediate and old stars can be as high as 60%, with a typical value of $\sim$40%.

The calibration of the different tracers implies the assumption of a star formation history. This could lead to discrepancies when comparing different tracers. As a measure of star formation history we use the Hα equivalent width. It is interesting to check if there is any systematic difference depending on age or star formation history. The equivalent width is defined as the quotient between the Hα flux, which measures the relevance of the recently formed population, and the continuum flux under the line (by wavelength unit), which measures the contribution of the stars that previously formed. It is also related to the age of the star-forming region (Pérez-González et al. 2003). In Figure 10, we show the $SFR_{FUV}/SFR_{H\alpha}$ ratio versus the Hα equivalent width. There exists an anti-correlation between both magnitudes, with the best fit given by

$$\log\left(\frac{SFR_{FUV}}{SFR_{H\alpha}}\right) = (1.45 \pm 0.64) - (0.72 \pm 0.29) \times \log(EW_{H\alpha}). \quad (11)$$

When the equivalent width is low, the weight of the young stars is less significant compared to that of the old population. In this case, UV provides higher SFRs than Hα, as it is more sensitive to older stars. As we move toward higher equivalent widths, the recently formed stars become more and more important than the old population. For the higher EW values, the UV subestimates the SFRs compared to Hα.

If we repeat this methodology regarding Hα and the IR, we obtain similar results. An anti-correlation exists between the ratio $SFR_{IR}/SFR_{H\alpha}$ and EW(Hα) (see Figure 11), which is described by the best linear fit as

$$\log\left(\frac{SFR_{IR}}{SFR_{H\alpha}}\right) = (1.09 \pm 0.76) - (0.52 \pm 0.35) \times \log(EW_{H\alpha}). \quad (12)$$

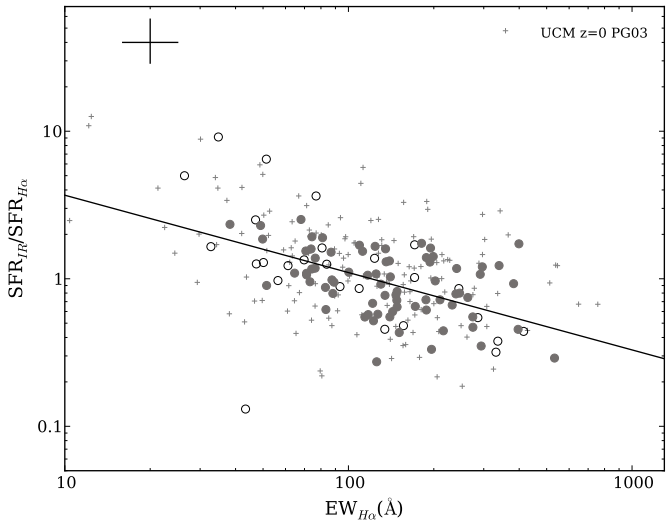

Figure 11. $SFR_{IR}/SFR_{H\alpha}$ ratio vs. EW(Hα). The line is the best linear fit to the data in logarithmic scale. The high EW(Hα) objects tend to have lower $SFR_{IR}/SFR_{H\alpha}$ ratios, whereas the lower EW(Hα) objects tend to have higher ratios. The crosses represent the UCM sample of local star-forming galaxies, which show the same trend.

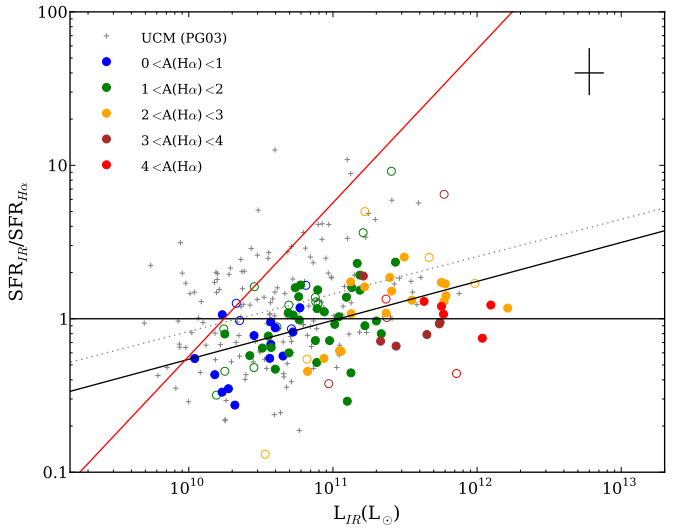

Figure 12. $SFR_{IR}/SFR_{H\alpha}$ ratio as a function of IR luminosity. The extinction is color-coded, as can be seen in the legend. The filled circles are confirmed by spectroscopy, whereas the open circles are not. The thick line represents the best linear fit to the data (see the text). The red line is our selection limit. We could detect only objects below this line. The UCM local sample of star-forming galaxies is represented by the crosses. The dotted gray line is the best linear fit to this sample.

Again, as we move toward higher EW(Hα), i.e., to higher contributions of young stars, the $SFR_{IR}/SFR_{H\alpha}$ ratio decreases. We have also plotted the local UCM sample of star-forming galaxies. These galaxies are located in the same region as the $z \sim 0.84$ sample, so the effect of the star formation history on the $SFR_{IR}/SFR_{H\alpha}$ ratio is similar at both redshifts. In both cases, constraining to the spectroscopically confirmed sample yields compatible results within errors. We note that the significance of both relations is not very high as errors are largely due to measurement errors, different star formation histories, etc.

Several authors (Pérez-González 2003; Flores et al. 2004; Hammer et al. 2005) found a correlation between this ratio and the IR luminosity in the local universe. The authors argued that the more luminous a galaxy is in the infrared, the more it is affected by extinction, to the point that the optical tracers could lose an important fraction of star formation, with some regions totally obscured by extinction. This would explain the subestimation of the SFR when measured by optical estimators, even when applying extinction corrections. At a higher redshift, Cardiel et al. (2003) found a similar behavior for their sample at $z = 0.8$. In Figure 12, we represent the $SFR_{IR}/SFR_{H\alpha}$ ratio versus the infrared luminosity L_{IR}(8–1000 μm). We find the same behavior reported by these authors: the Hα estimator starts to subestimate the SFR (with respect to IR) when we move to higher L_{IR}(8–1000 μm). The dependency is not a selection effect as the limits of our sample would allow us to detect galaxies with higher and lower ratios (see figure). No dependency is found between the extinction of the objects (coded with different colors in the figure) and the degree of subestimation. One would expect some kind of dependency, as the obscured regions in the optical are visible in the IR, although it does not negate this scenario.

The best linear fit, excluding the 5% extreme values, is given by

$$\log\left(\frac{SFR_{IR}}{SFR_{H\alpha}}\right) = -(2.61\pm2.17)+(0.23\pm0.19)\times\log\left(\frac{L_{IR}}{L_\odot}\right), \quad (13)$$

which can be seen in the figure as a thick line.

This result agrees with previous results, with the IR providing higher SFRs as we move toward higher IR luminosities. We note that uncertainties are large and in this case, in which we are representing x/y versus x, a small correlation would arise from random scatter. However, the slope of such a correlation is always below 0.1 within the range of our values, as we have checked by generating random samples. We have plotted the UCM local sample as a reference, with its best linear fit as a dotted line in Figure 12. Both samples present very similar slopes when fitted, but there is an offset between them. For the UCM sample, the IR starts to provide higher SFRs for lower IR luminosities than for the $z \sim 0.84$ sample. If we consider that the change in the $SFR_{IR}/SFR_{H\alpha}$ ratio is due to the increment of Hα luminosity that is totally obscured by dust, at higher IR luminosity more regions would be totally obscured by dust. Then, the difference between the local relation and that at $z \sim 0.84$ presented in Figure 12 could be explained by a change in the number and size of star-forming regions. These should be less numerous, although larger, at $z = 0.84$, given that SFRs are higher in the sample at $z = 0.84$ than in the local sample. Thus, Hα luminosity would be higher for each region, and the dust would not totally attenuate that region. The total attenuation in the optical of some star forming regions would only take place in galaxies with high IR luminosity and large amounts of dust.

Thus, we have two possible effects that could explain the scatter when comparing SFRs coming from Hα and IR: (1) contribution of the evolved population and (2) the presence of star-forming regions totally attenuated by dust.

However, Figure 12 can be explained by taking into account the contribution of the evolved population to the IR. We have shown that the $SFR_{IR}/SFR_{H\alpha}$ ratio increases with the IR luminosity and that there is an offset in that relation between the local universe and $z \sim 0.84$. However, the dependency of that ratio with the EW(Hα), i.e., with the weighted age, is independent of redshift. Then, we can consider that the same $SFR_{IR}/SFR_{H\alpha}$ ratio implies the same weighted age at $z = 0$ and at $z \sim 0.84$. On the other hand, galaxies with the same

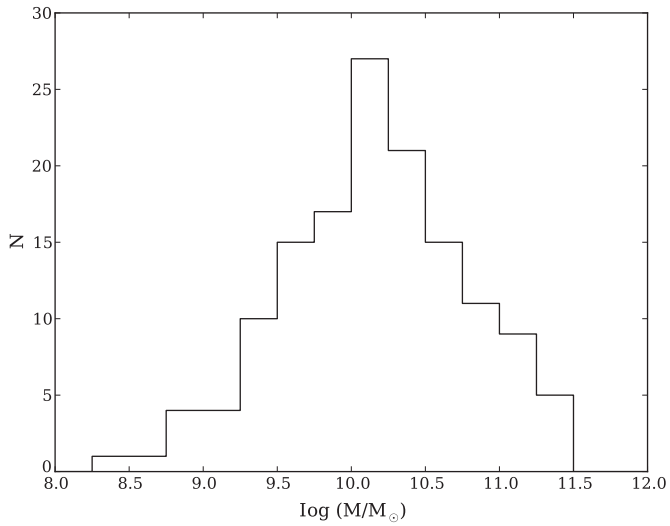

Figure 13. Histogram of stellar masses for our sample. The completeness falls below $10^{10}\,M_\odot$.

weighted age have higher infrared luminosity at $z = 0.84$ than at $z = 0$, as depicted in Figure 12. As their IR luminosity is higher, the SFR is higher and, as the weighted age is the same, the underlying population has to be more luminous, i.e., more massive. This is in agreement with what can be expected from the *downsizing* (Cowie et al. 1996) scenario, where star formation moves from more massive galaxies at higher redshifts to less massive galaxies at lower redshifts (see Section 6).

Although the effect of age could explain the observed difference, both age and extreme attenuation of some regions probably contribute.

6. STELLAR MASSES

The stellar mass is one of the most important properties of a galaxy, as it provides a robust measurement of the scale of the galaxy and is also an indicator of past star formation. The estimate of stellar mass is obtained from the best-fitting template to the SED of each galaxy. The template provides mass-to-light ratios for each observed band, and a stellar mass is computed for each one. The final value is the average of the values obtained for each observed band, the associated error being the standard deviation of the distribution of stellar masses. The results are more reliable than those obtained through a single mass-to-light ratio, as it is less sensitive to the star formation history or errors in photometry or templates. For more details on the procedure, see Pérez-González et al. (2008) and Barro et al. (2011b).

Stellar masses were obtained with the PEGASE 2.0 (Fioc & Rocca-Volmerange 1997) stellar population synthesis models, a Salpeter (1955) IMF, and the Calzetti et al. (2000) extinction law. Different stellar population models (Bruzual & Charlot 2003; Maraston 2005), IMFs (Kroupa 2001; Chabrier 2003), or extinction laws will provide different estimates. The models used here predict the largest stellar masses, although all models are roughly consistent within a factor of two. For a detailed comparison between the different models, we refer the reader to Barro et al. (2011b).

In Figure 13 we present the histogram of masses for our sample. The median and standard deviation for the distribution is $M_\star = 1.4^{+4.6}_{-1.1} \times 10^{10} M_\odot$. At the same redshift, the typical mass found by Pérez-González et al. (2008) for an IRAC selected sample is $M^*_\star = 1.6 \times 10^{11}\,M_\odot$. The typical mass of a star-forming galaxy (to the limit of our sample) is ten times lower than the typical mass of the global population of galaxies. Sobral et al. (2011, hereafter S11) find a typical mass $M_\star = 2.25 \times 10^{10}\,M_\odot$ (after scaling from a Chabrier to a Salpeter IMF) for their HiZELS sample at $z = 0.84$, in very good agreement with ours, given that both limiting fluxes are very similar.

The loss of the low-mass population of star-forming galaxies is clear in the histogram, with the number of galaxies starting to decrease below $\sim 10^{10}\,M_\odot$. This effect is produced by the limiting line flux reached in our selection process, given the correlation between stellar mass and star formation found in the local universe (Brinchmann et al. 2004, hereafter B04) and at higher redshifts up to $z \sim 6$ (Noeske et al. 2007b; Elbaz et al. 2007; Daddi et al. 2007; Stark et al. 2009).

The SFR–$M_\star$ correlation for our sample is shown in Figure 14, where the Hα SFR versus the stellar mass is represented. The completeness level (red dashed line) is estimated performing simulations of the whole selection process and taking into account the extinction. This process involves several steps that are explained in detail in the Appendix. The SFR–$M_\star$ relations obtained from Dutton et al. (2010), from the samples presented in Noeske et al. (2007b) at $z \sim 0.8$, and in Elbaz et al. (2007) at $z \sim 1.0$, in good agreement with our sample, are overplotted. In addition, the UCM local sample of star-forming galaxies (Pérez-González et al. 2003) and the SDSS DR4 galaxies classified as star forming in B04 are also shown. The slope for these samples is similar to ours, although the SDSS is steeper. There is a shift in SFR between the local ones and that at $z \sim 0.84$. For a given mass the sample at $z \sim 0.84$ presents higher ($\sim \times 5.5$) SFRs than the local sample. Another way to see it is that for a given SFR the galaxies in the past were less massive than local galaxies. This difference between the local universe and $z \sim 0.84$ clearly shows that star formation changes as the universe evolves. Contrary to our result, S11 do not find any relation between SFR and stellar mass. This is intriguing, as the selection technique and line flux reached are very similar in both surveys.

In this type of comparison between our sample and the local samples, one could think we are just watching the tail of the distribution for the $z \sim 0.84$ sample, which leads us to the inaccurate conclusion that an evolutionary effect is present. In V08 we computed the Hα luminosity function (LF) and we also estimated the completeness limit. The results showed that we start to lose a substantial fraction of objects one order of magnitude below L^*(Hα) (obtained from the LF fit to a Schechter function). We were 50% complete for $\log L(\mathrm{H}\alpha) > 42.0$, which in terms of $L^*(\mathrm{H}\alpha)$ is $\log(L(\mathrm{H}\alpha)/L^*(\mathrm{H}\alpha)) \sim -1.0$. Therefore, we conclude that we are not observing the rare galaxies in the tail of the distribution. On the other hand, the UCM sample is considered complete down to $\log L(\mathrm{H}\alpha) \sim 40.7$, which in terms of $L^*(\mathrm{H}\alpha)$ (for this redshift) is $\log\,(L(\mathrm{H}\alpha)/L^*(\mathrm{H}\alpha)) \sim -1.2$. Thus, we are reaching very similar Hα luminosities for both samples in terms of $L^*(\mathrm{H}\alpha)$. Another argument supporting this conclusion is that we detect essentially the same population as those in samples selected in UV or IR at the same redshift (see V08).

It is also interesting to compare with a sample selected purely by stellar mass, as that presented in Pérez-González et al. (2008). The median values of this sample at $z = 0.8$–1.0 fall very close to our best fit, being compatible within errors. However, the difference between our best fit and the median values of that sample increases as we move to higher masses, presenting the mass selected sample with lower SFRs. Although this trend is very weak and, given the errors, could even not be present, it

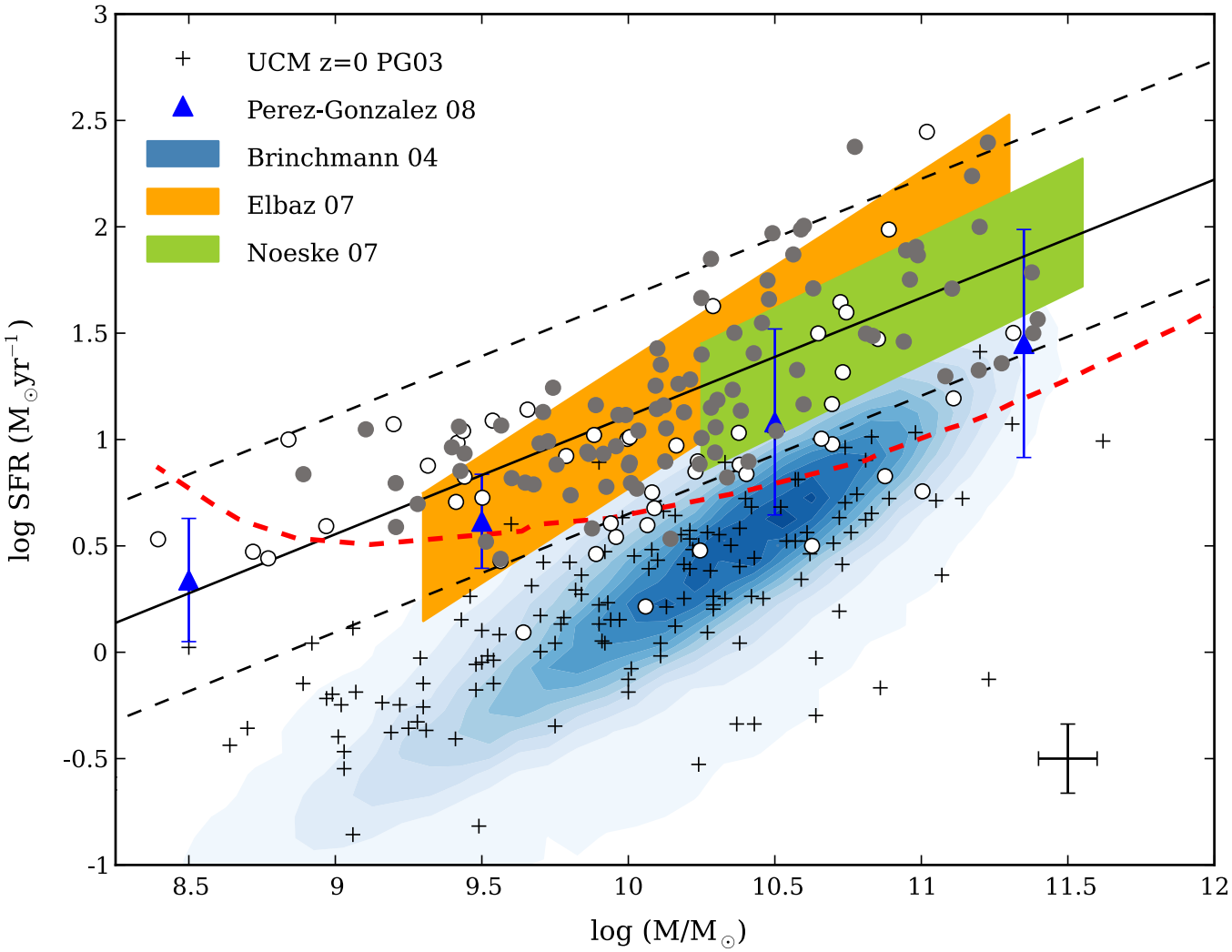

Figure 14. Hα star formation rate vs. mass. The circles represent our sample: filled for the spectroscopic confirmations and open for the remainder. The red dashed line represents a 50% completeness level. The best fit within mass completeness limits is shown as a solid line, with the dashed lines enclosing 90% of the data. The filled regions are the best fits obtained by Elbaz et al. (2007) and Noeske et al. (2007b; compiled in Dutton et al. 2010). The mass selected sample values at $z = 0.8$–1.0 obtained by Pérez-González et al. (2008, PG08) are represented by the blue crosses. The UCM (crosses) and SDSS (blue color map) local samples are also shown.

is consistent with the *downsizing* scenario (Cowie et al. 1996): the fraction of galaxies with very low star formation seems to increase as we move to higher masses, with the median SFR decreasing in the mass selected sample. At low masses, the effect is less pronounced, as galaxies are undergoing strong star formation episodes and are still very active in general.

The SFR–$M_\star$ correlation allows us to estimate the mass range in which we can consider our sample unbiased. The cut between the SFR 50% completeness level and the lower envelope in the SFR–$M_\star$ distribution gives us the stellar mass range within which we can consider our sample free of biases. The lower envelope is the best linear fit shifted downward to enclose 95% of the data confirmed by spectroscopy (90% within the lower and upper envelopes). In practice, it is an iterative process: first we fit the data above and below initial mass limits, then we find the new mass limits in the intersection between the lower envelope and the completeness curve, and the procedure is repeated until the new and initial mass limits converge to the same value. This gives us a lower limit of $\sim 10^{10}\ M_\odot$ and no upper limit, indicating that we are limited by explored volume on the upper side, as we do not detect any galaxy above $\sim 3 \times 10^{11}\ M_\odot$. As mentioned before, the derived correlation is in good agreement with Noeske et al. (2007b) and Elbaz et al. (2007), both at a similar redshift. Moreover, we find that the scatter is $\sim$0.3 dex, which is the typical value found in other studies and seems to be almost constant with redshift (Dutton et al. 2010). However, the lower envelope and the 50% completeness limit are close; thus, it is still possible that the observed correlation is produced by the selection effect. To rule out this possibility we simulate fake samples of galaxies following different SFR–M^* relations. First, we simulate a population of galaxies following the linear relation derived from our sample. We assign to each galaxy a random stellar mass. Given this stellar mass we compute the SFR with the linear relation derived from the real sample, adding Gaussian noise to simulate the scatter ($\sigma = 0.3$). Once we have this fake population we check whether the galaxies would be detected considering the completeness curves (measured for different completeness levels) and the volume sampled. After repeating the fitting process considering the completeness curve as well as the lower envelope, we find that the results are in good agreement with the input, with relative errors within 10% for the slope and 20% for the constant term. The same process is repeated 20 times to avoid biases due to rare distributions. When a flatter relation (20% less steep) is used we find similar results,

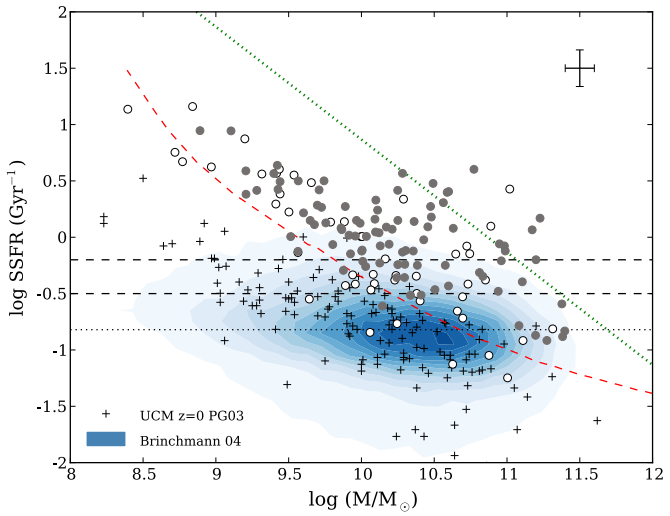

Figure 15. Specific Hα star formation rate vs. mass. The circles represent our sample: filled for the spectroscopic confirmations and open for the remainder. Our 50% completeness level is represented by the red dashed line. The diagonal dotted line is the place that would occupy the objects with $L(\mathrm{H}\alpha) = L^*(\mathrm{H}\alpha)$. The crosses represent the UCM sample of local star-forming galaxies. The color map shows the values for the SDSS sample. The horizontal dashed lines indicate the values of sSFR at which $b = 1$ and $b = 2$ at $z = 0.84$. The dotted lines are the same but for the local universe and $b = 1$. The line for $b = 2$ coincides with the $b = 1$ line for $z = 0.84$.

although in some cases the lower envelope is so low that it does not cut the completeness curve and no measure can be obtained. Given the SFR–$M_\star$ relation and the limits of our sample, we can be confident that we will not introduce any substantial bias when inferring mass related properties using the sample within those mass limits.

Figure 14 could be interpreted as going against *downsizing*, as galaxies at $z \sim 0.84$ have higher SFRs than local ones, independent of stellar mass. The key concept here is not the absolute SFR, but the sSFR, which is the SFR per unit of stellar mass, and thus is a good indicator of the impact that the star formation has in the galaxy. In Figure 15, we represent the sSFR for our sample and for the SDSS and UCM local samples. Now the change in star formation as we move toward the local universe and the shift in star formation from more massive to less massive galaxies are clear, considering the evolutionary impact of the SFR processes.

There exists an anti-correlation between the sSFR and the stellar mass, evidence that star formation processes have a higher impact on less massive galaxies. This trend is also present in the star-forming galaxies of the local universe, with a similar slope in the case of the UCM sample, although it is shifted in the sSFR axis to lower values, indicating that the star formation is less important. Most of our sample falls below the line (green dotted line) where the $L^*(\mathrm{H}\alpha)$ galaxies would lie at that redshift, which shows that we are not missing the general population. Previous determinations (e.g., Pérez-González et al. 2005; Noeske et al. 2007a; Rodighiero et al. 2010; S11) already found this relation, but discrepancies arise regarding the slope of the correlation. Rodighiero et al. (2010), through IR SFR estimations, found a flatter relation compared to Noeske et al. (2007a), who used UV–optical SFR estimators. In contrast, S11 found a much steeper relationship, with a slope ∼–1, given that these authors do not find any correlation between SFR and mass.

The slope for our sample (computed only for objects within our mass limits) is $\beta = -0.4 \pm 0.1$, which is in good agreement with that of Noeske et al. (2007b), but steeper than the value obtained by Rodighiero et al. (2010, $\beta = -0.28$) in the redshift range $0.5 < z < 1.0$. This discrepancy could come from the different selection criteria. While in this paper galaxies are selected purely by star formation, Rodighiero et al. analyzed a sample selected by mass through the IRAC 4.5 μm band, with a color cut to avoid the inclusion of red-sequence galaxies, although they try to recover dusty starbursts that might fall in the red sequence. In this work we have not excluded any galaxy by its color since, as we have shown, most of the red-sequence galaxies were in fact dusty star-forming galaxies. In line with this hypothesis, Karim et al. (2011) found a slope similar to ours ($\beta = -0.38$) using a sample of star-forming galaxies selected from a mass selected sample in the IRAC 3.6 μm band. However, in this case the authors classify the objects as star-forming if they belong to the blue cloud, once the attenuation has been removed. Gilbank et al. (2011) have found very recently a very similar value for the slope ($\beta = -0.42$) using a spectroscopic sample with [O II] SFRs around $z \sim 1$.

The birth rate parameter b is linked to the sSFR as

$$b = \frac{\mathrm{SFR}}{\langle \mathrm{SFR} \rangle} = \mathrm{SFR}\frac{t_f}{2 \times M_*}, \quad (14)$$

where $\langle \mathrm{SFR} \rangle$ is the average star formation in the whole history of the galaxy, or, in other words, the average SFR that would have produced the current stellar mass. Thus, we can obtain this average star formation by dividing the stellar mass M_* by the elapsed time since the galaxy formed t_f. The factor of two takes into account the stellar mass returned to the interstellar medium. The parameter depends on the choice of the beginning of star formation, but it is still very interesting when comparing populations at different redshifts. In this work we set this initial time at the beginning of the universe, $t_f = 6.5$ Gyr for $z = 0.84$ and $t_f = 13.4$ Gyr for the local universe. A galaxy with a value of b higher than one tells us that the current star formation is more intense than the average star formation in the past. A value of two indicates an especially intense star formation episode.

Most of our galaxy sample presents values of b higher than one, with 85% (119/140) with $b > 1$ and 66% (92/140) with $b > 2$. In the local universe, the SDSS and UCM samples show a very different scenario. Half the SDSS sample (48%) has b values over one and only 16% above two. The UCM sample presents similar results, with 58% of the sample with $b > 1$ and 25% with $b > 2$. If we confine the analysis to the most massive galaxies (with stellar masses above $10^{11}\,M_\odot$) within our sample, 36% (5/14) of these have b values above one, and 29% (4/14) have values over two. Regarding the local samples, the proportions are very different, with 20% in the case of the SDSS, 14% in the case of the UCM with b over one, only 3% with b over two within the SDSS sample, and none in the UCM sample. This is direct evidence of *downsizing*, as the fraction of most massive galaxies with intense ($b > 1$) or very intense ($b > 2$) star formation was higher in the past, and has reduced dramatically from that epoch to the present.

6.1. Quenching Mass

The star formation mass relation holds up until a certain mass, above which it no longer holds and the star formation drops sharply (see, for example, B04). Galaxies above this mass are considered quiescent, as star formation processes are no longer the main drivers of its evolution and they move to the red sequence. Therefore, this mass defines an upper limit for the stellar mass of the galaxies actively forming stars. Bundy

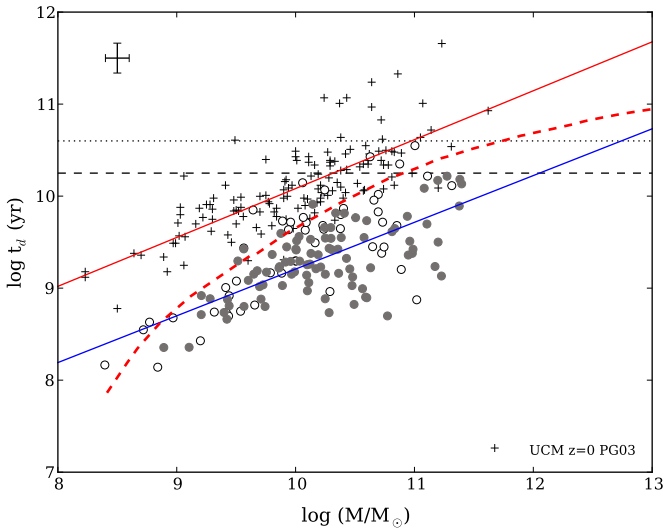

Figure 16. Doubling time t_d vs. stellar mass. The circles represent our sample: filled for the spectroscopic confirmations and open for the remainder. The 50% completeness level is represented by the red dashed line. The crosses represent the UCM local sample of star-forming galaxies. The dashed horizontal line indicates the doubling time at which we consider a galaxy at $z = 0.84$ as quiescent. The dotted horizontal line represents the same but for the local universe. Best linear fits computed for both samples are also shown.

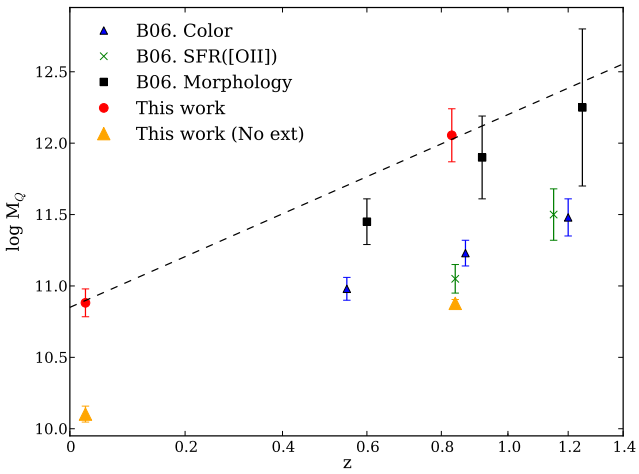

Figure 17. Evolution of the quenching mass limit M_Q. Red circles represent the results obtained in this work for the Hα selected samples at $z \sim 0.84$ and the local universe. The orange circles are the estimated quenching masses when no extinction correction is considered. The rest of the points correspond to the B06 work according to the different criteria employed: black squares for morphology, green crosses for [O II] λ3727 SFRs, and blue triangles for the $(U - B)$ color.

et al. (2006, hereafter B06) found that this *quenching* mass evolves with redshift, increasing as we move to higher redshift, as expected in the *downsizing* scenario. In this work, we use our Hα selected samples to study this *quenching* mass evolution, which our star-forming samples also reflect. The decrease of sSFR with mass implies that galaxies will eventually reach a mass over which the star formation processes will be very low and we can consider them quiescent. The observed shift between both trends leads to a different *quenching* mass that is lower than that at the local universe.

With our data it is possible to estimate an upper limit for the *quenching* mass. For the sake of clarity we are going to use the *doubling* time t_d, which is analogous to the sSFR and is defined as

$$t_d = \frac{M_*}{\mathrm{SFR}(1-\mathrm{R})} = \frac{1}{\mathrm{sSFR}(1-R)}, \quad (15)$$

where R is the fraction of mass returned to the interstellar medium, which is generally assumed to be ~0.5 (Bell 2003).

The *doubling* time tells us how long it will take for that galaxy to duplicate its stellar mass if its current star formation stays constant. Galaxies with a high *doubling* time will evolve slowly, whereas galaxies with a low one will evolve quickly. *Doubling* time versus mass for our sample and the local UCM sample is shown in Figure 16. In order to estimate the *quenching* mass we define a galaxy as quiescent if its *doubling* time is higher than what we define as *quenching* time: $t_Q = 3 \times t_H$, where t_H is the Hubble time. To obtain the typical mass that corresponds to the *quenching* time we performed several steps. First, we simulated 1000 realizations of our sample, varying randomly the values of SFR and mass within twice the errors, i.e., each object will have values randomly distributed in the intervals $[M - 2\Delta M, M + 2\Delta M]$ and $[\mathrm{SFR}_{\mathrm{H}\alpha} - 2\Delta\mathrm{SFR}_{\mathrm{H}\alpha}, \mathrm{SFR}_{\mathrm{H}\alpha}+2\Delta\mathrm{SFR}_{\mathrm{H}\alpha}]$. Second, we do a linear fit of t_d versus mass only with the objects whose simulated mass falls above our mass limit. For each of these fits we compute the *quenching* mass as the mass at which the *doubling* time t_d is equal to the *quenching* time t_Q. The final *quenching* mass M_Q is the median of the whole distribution of *quenching masses*, with the error determined by the standard deviation of the distribution. The same process has been followed for the UCM sample.

We obtain that $M_Q = 1.0^{+0.6}_{-0.4} \times 10^{12}\, M_\odot$ ($\log(M_Q/M_\odot) = 12.0 \pm 0.2$) for the $z \sim 0.84$ sample and $M_Q = 7.9^{+1.9}_{-1.5} \times 10^{10}\, M_\odot$ ($\log(M_Q/M_\odot) = 10.9 \pm 0.1$) for the local sample. If we consider only the spectroscopically confirmed sample we obtain $\log(M_Q/M_\odot) = 12.2 \pm 0.2$, slightly higher although compatible within errors. In the case of $z \sim 0.84$ the *quenching* mass is outside the range of masses detected, given the limit on the detection of massive galaxies imposed by the sampled volume and the equivalent width limit of the survey, which prevents us from selecting objects with lower sSFRs. These masses are upper limits, given that at high stellar masses the correlation between *doubling* time and mass will break as a consequence of *quenching*. Galaxies with higher t_d than predicted by the correlation will appear as the *quenching* takes over, possibly lowering the average *quenching* mass, especially in the case of $z \sim 0.84$, where no galaxies around M_Q have been detected. In order to detect these galaxies it would be necessary to survey larger volumes. In addition, the simulations (see Section 6) show that we may overestimate the quenching mass at $z \sim 0.84$ by ~0.1 dex, due to completeness limits. However, these simulations also show that we would be able to detect quenching masses ~0.5 dex lower (SFR–M_* slope 20% lower), with a similar dispersion.

Our *quenching* mass estimation for the local universe is in very good agreement with the stellar mass ($\sim 7 \times 10^{10}\, M_\odot$; scaled from a Kroupa to a Salpeter IMF) above which Kauffmann et al. (2003) found a rapid increase in the fraction of galaxies with old populations in the SDSS local sample. This change, detected by a transition from lower values of $D_n(4000)$ to higher values, is also seen as a change in the slope of the μ_*–M_* (surface stellar mass density versus stellar mass) correlation. Our result at $z \sim 0.84$ is higher than those estimated by B06 at a similar redshift. In their work, they used three different approaches: morphology, $U - B$ color, and SFRs derived from [O II] equivalent width. Through the morphology criterion they obtained $M_Q \sim 8 \times 10^{11}\, M_\odot$, whereas both color and SFR criteria provide lower masses $\sim 10^{11}\, M_\odot$ (see Figure 17). We have scaled B06 masses from the Chabrier IMF

to the Salpeter IMF used in this work, adding 0.25 dex. Our result is in good agreement with their morphology-based estimation, but it is higher than those based on color or SFR. B06 attributed this difference to a longer timescale in the processes that transform late types into early types. However, our value is solely based on star formation and no morphology considerations have been done. One of the caveats of their SFR and color measurements is that extinction was not corrected. Therefore, dusty starbursts would appear redder and with lower SFRs, as they would be classified as red or non-star-forming galaxies, which translates into lower quenching masses. If we again estimate M_Q for our Hα selected samples, this time without applying the extinction correction, we obtain lower values: $M_Q = 7.6^{+1.7}_{-1.4}\times10^{10}\,M_\odot$ log $M_Q/M_\odot = 10.88 \pm 0.09$) for the $z \sim 0.84$ sample and $M_Q = 1.3^{+0.2}_{-0.2}\times10^{10}\,M_\odot$ (log $M_Q/M_\odot = 10.13 \pm 0.05$) for the local sample. The effect of the extinction is very high and is enough to account for the difference between B06 morphology and color/SFR estimations. Our result is also consistent with the work by Pérez-González et al. (2008), in which they found that at $z \sim 0.8$ all the stellar mass has already been assembled for objects more massive than $M_\star = 10^{12}\,M_\odot$ and almost fully assembled for objects with stellar mass in the range $10^{11.7}$–$10^{12}\,M_\odot$.

The *quenching* masses estimated through this method rely on the definition of t_Q; however, independently of this parameter, we find a strong evolution between the local universe and $z \sim 0.84$. In the local universe, galaxies with masses higher than $10^{11}\,M_\odot$ are quiescent, and their evolution is limited to interactions with other galaxies via dry mergers (or other processes not involving massive star formation), whereas at $z \sim 0.84$, galaxies with mass in the range $\sim10^{11}$to $\sim10^{12}\,M_\odot$ are still under strong star formation processes. This is, again, in good agreement with the *downsizing* scenario. Despite the fact that we do not have enough data to constrain the M_Q evolution with redshift, we find that our results are compatible with the parameterization given by B06, i.e., $M_Q \propto(1+z)^{4.5}$. The added value is that we have extended the redshift baseline to the local universe, using samples selected uniformly.

7. SUMMARY AND CONCLUSIONS

In this work we have analyzed the properties of an Hα selected sample of star-forming galaxies at $z \sim 0.84$, focusing on star formation and stellar mass.

We have discarded the AGN contaminants through two criteria: X-ray luminosities and IRAC colors. We find seven counterparts in X-ray, though three of them present very low fluxes, compatible with originating from star formation processes. Thus, we only discard the four objects with fluxes high enough to have an AGN origin. Using IRAC colors we find another 10 objects (one of them already detected in X-rays) that fulfill the criterion to be considered AGNs. A total of 13 objects are finally discarded.

The objects of our sample present a median $M_B = -20\overset{\text{m}}{.}5 \pm 0\overset{\text{m}}{.}9$, brighter by more than one magnitude than the UCM local sample of star-forming galaxies. Most of the galaxies belong to the blue sequence, with a small fraction of objects in the green valley and the red sequence. Once the extinction corrections are applied, all except two red objects move to the blue sequence, unveiling their dusty nature.

A check on the extinction law reveals that the Calzetti et al. (2000) extinction law is appropriate for our objects, but with $E(B-V)_{\rm stars} = 0.55\,E(B-V)_{\rm gas}$.

The Hα SFR, without applying the extinction correction, presents values in the range 2–10 $M_\odot$. We have also estimated SFRs with FUV and IR. In the first case, the non-extinction-corrected FUV underestimates the SFR with respect to Hα. The opposite case is given for the IR, which overestimates the SFR with respect to Hα. These discrepancies are mainly driven by the extinction. Once we apply the extinction correction to both FUV and Hα estimations, all SFR tracers agree within a factor of three, and the highest SFRs reach several hundreds solar masses per year.

The scattering between the different tracers is correlated with the Hα equivalent width. This can be explained through the different weighted ages of the objects (which is related to the EW) and the fact that FUV and IR SFRs are sensitive to a longer time range than Hα and are more affected by older populations.

We have estimated stellar masses for our sample, finding that the median value is $M_\star = 1.4^{+4.6}_{-1.1}\times10^{10}\,M_\odot$, in good agreement with the result obtained by S11 for a sample selected with criteria similar to ours. The typical mass found by Pérez-González et al. (2008) for an IRAC selected sample at this redshift is ten times higher than this value.

Our sample shows a trend between SFR and stellar mass. The slope of this trend is in good agreement with the value obtained by Noeske et al. (2007a) and is flatter than the Elbaz et al. (2007) result. The trend is very similar to that of the local universe, although it is shifted to higher values of SFR. This indicates that, for the same stellar mass M_*, star-forming galaxies at $z \sim 0.84$ are under stronger star formation episodes than their local analogous galaxies.

The sSFR shows a negative correlation with stellar mass. The star formation in more massive galaxies, although there is a higher SFR, has less impact than that in less massive ones, due to the large stellar mass already formed. The same trend is observed in the local universe, though it is shifted to lower sSFRs. This is in good agreement with the *downsizing* scenario, in which massive galaxies are formed earlier than less massive ones. The fraction of massive galaxies ($M_* > 10^{11}\,M_\odot$) undergoing strong star formation processes ($b>2$), $\sim$29% at $z \sim 0.84$ against $<$3% at the local universe, also supports this scenario.

Finally, we have quantified the *downsizing*, estimating the *quenching* mass at $z \sim 0.84$ and at the local universe based on the Hα SFR. We find that $M_Q = 1.0^{+0.6}_{-0.4}\times10^{12}\,M_\odot$ (log $(M_Q/M_\odot) = 12.0 \pm 0.2$) at $z \sim 0.84$ and $M_Q = 7.9^{+1.9}_{-1.5}\times10^{10}\,M_\odot$ (log $(M_Q/M_\odot) = 10.9 \pm 0.1$) in the local universe. The evolution since the local universe is out of doubt, with an increase in the *quenching* mass of an order of magnitude.

We thank Armando Gil de Paz for helpful discussions and comments. We acknowledge support from the Spanish Programa Nacional de Astronomía y Astrofísica under grant AYA2009-10368. Partially funded by the Spanish MICINN under the Consolider-Ingenio 2010 Program grant CSD2006-00070: First Science with the GTC. V.V. acknowledges support from the AstroMadrid Program CAM S2009/ESP-1496: "Astrofísica y Desarrollos Tecnológicos en la Comunidad de Madrid" funded by the Comunidad de Madrid and the European Union. P.G.P.-G. acknowledges support from the Ramón y Cajal Program financed by the Spanish Government and the European Union. This work is based in part on observations made with the *Spitzer Space Telescope*, which is operated by the Jet Propulsion Laboratory, Caltech under NASA contract 1407. *GALEX* is a NASA Small Explorer launched in 2003 April. We gratefully acknowledge NASA's support for construction,

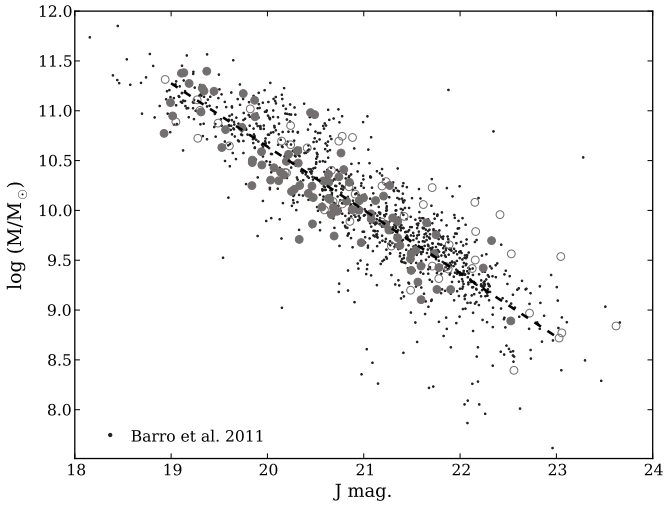

Figure 18. Stellar mass vs. J-band magnitude. The circles represent our sample: filled for the spectroscopic confirmations and open for the remainder. The small dots are the objects within our redshift range from the Barro et al. (2011a) mass selected sample. The dashed line is the best linear fit for the mass selected sample.

operation, and scientific analysis of the *GALEX* mission. This research has made use of the NASA/IPAC Extragalactic Database (NED) which is operated by the Jet Propulsion Laboratory, California Institute of Technology, under contract with the National Aeronautics and Space Administration. Based in part on data collected at Subaru Telescope and obtained from the SMOKA, which is operated by the Astronomy Data Center, National Astronomical Observatory of Japan. We acknowledge Edward L. Wright for his World Wide Web Cosmology Calculator (Wright 2006), which has been used during the preparation of this paper.

APPENDIX

COMPLETENESS LEVEL AS A FUNCTION OF STELLAR MASS

The SFR completeness level for our sample depends on the stellar mass, due to the selection process, which is basically a selection in equivalent width. In V08 we simulated the selection process to determine the completeness level versus the line flux, but without considering the dependence on stellar masses, as it was unnecessary. The process consisted of the introduction of simulated galaxies to the real images to check whether or not they were recovered by the selection method. Fake galaxies were created with different line and continuum fluxes, sizes, and inclinations in the real images. The outcome was the line flux completeness level.

The problem we need to address here is at which SFR, corrected for attenuation, the completeness level is 50% as a function of stellar mass. The main problem is that we need to relate the stellar mass and extinction to the observables, i.e., the broadband and narrowband magnitudes. Intuitively, one may think that there exists a correlation between the stellar mass and the broadband magnitude. Indeed, as can be seen in Figure 18, there is a correlation between the stellar mass and the J magnitude for our sample. However, it might be affected by selection biases, so we also check this relation against another sample. For this double-check we use the mass selected sample from the AEGIS database presented in Barro et al. (2011a) and Barro et al. (2011b). If we take all the objects with spectroscopic redshift within the limits of our sample, we obtain a very similar relation. The best fit to the data gives $M^* = 23.36–0.636\ M_J$.

With this correlation we can assign a stellar mass for an object given its J-band flux. Thus, we can check the fraction of objects selected for a certain line-flux, defined by their emission in the broadband and narrowband filters, and a stellar mass, estimated from the broadband flux. The line flux is transformed to SFR applying the corresponding calibration (Equation (1)) and applying a mean correction for the nitrogen contribution ($I([N\,\textsc{ii}]\,\lambda6584)/I(\mathrm{H}\alpha) = 0.26$). At the end we have a completeness level for each combination of SFR and stellar mass. From this we can obtain the SFR 50% completeness level as a function of mass.

However, this completeness does not take into account the attenuation affecting the SFR measurement. To correct this effect we can apply the extinction correction to the SFR completeness level as follows:

$$\mathrm{SFR}(M^*)^{\mathrm{corrected}}_{50\%} = \mathrm{SFR}(M^*)^{\mathrm{uncorrected}}_{50\%}\ 10^{0.4\,A(\mathrm{H}\alpha)}, \quad \text{(A1)}$$

where $\mathrm{SFR}(M^*)^{\mathrm{uncorrected}}_{50\%}$ is the Hα SFR for which we are 50% complete at stellar mass M^*.

The question that arises now is which amount of extinction to apply. The immediate solution is to apply the mean (median) extinction correction obtained for the sample. However, it is well known that the amount of extinction depends on the total SFR. This fact has been shown for the Sobral et al. (2009) sample by Garn et al. (2010). In particular, these authors find that $A(\mathrm{H}\alpha) = 0.73 + 0.44 \log \mathrm{SFR(IR)}$. As we saw in Section 5.2.2, we can assume that the IR-derived SFR is equal to the extinction-corrected Hα SFR, and thus we can write

$$\mathrm{SFR}(M^*)^{\mathrm{corrected}}_{50\%} = \mathrm{SFR}(M^*)^{\mathrm{uncorrected}}_{50\%}\ 10^{0.4\,(a+b\times\log \mathrm{SFR}(M^*)^{\mathrm{corrected}}_{50\%})} \quad \text{(A2)}$$

$$= \mathrm{SFR}(M^*)^{\mathrm{uncorrected}}_{50\%}\ 10^{a'+b'\times\log \mathrm{SFR}(M^*)^{\mathrm{corrected}}_{50\%}} \quad \text{(A3)}$$

with $a = 0.73$, $b = 0.44$, $a' = 0.4 \times a$, and $b' = 0.4 \times b$. We can find the value of SFR, obtaining

$$\log \mathrm{SFR}(M^*)^{\mathrm{corrected}}_{50\%} = \frac{\log \mathrm{SFR}(M^*)^{\mathrm{uncorrected}}_{50\%} + a'}{1 - b'}. \quad \text{(A4)}$$

This equation gives us a completeness level of 50% considering that the extinction depends on the total SFR. The computed completeness curve is shown in Figure 14.

REFERENCES

Adelberger, K. L., Steidel, C. C., Shapley, A. E., et al. 2004, ApJ, 607, 226
Alexander, D. M., Bauer, F. E., Brandt, W. N., et al. 2003, AJ, 126, 539
Alonso-Herrero, A., Pérez-González, P. G., Alexander, D. M., et al. 2006, ApJ, 640, 167
Barmby, P., Huang, J., Ashby, M. L. N., et al. 2008, ApJS, 177, 431
Barro, G., Gallego, J., Pérez-González, P. G., et al. 2009, A&A, 494, 63
Barro, G., Pérez-González, P. G., Gallego, J., et al. 2011a, ApJS, 193, 13
Barro, G., Pérez-González, P. G., Gallego, J., et al. 2011b, ApJS, 193, 30
Bell, E. F. 2003, ApJ, 586, 794
Bouwens, R. J., Illingworth, G. D., Franx, M., et al. 2009, ApJ, 705, 936
Bouwens, R. J., Illingworth, G. D., Oesch, P. A., et al. 2010, arXiv:1006.4360
Brinchmann, J., Charlot, S., White, S. D. M., et al. 2004, MNRAS, 351, 1151 (B04)
Bruzual, G., & Charlot, S. 2003, MNRAS, 344, 1000

Bundy, K., Ellis, R. S., Conselice, C. J., et al. 2006, ApJ, 651, 120 (B06)
Calzetti, D., Armus, L., Bohlin, R. C., et al. 2000, ApJ, 533, 682
Calzetti, D., Kennicutt, R. C., Jr., Bianchi, L., et al. 2005, ApJ, 633, 871
Calzetti, D., Kennicutt, R. C., Engelbracht, C. W., et al. 2007, ApJ, 666, 870
Capak, P., Cowie, L. L., Hu, E. M., et al. 2004, AJ, 127, 180
Caputi, K. I., Dole, H., Lagache, G., et al. 2006, ApJ, 637, 727
Cardelli, J. A., Clayton, G. C., & Mathis, J. S. 1989, ApJ, 345, 245
Cardiel, N., Elbaz, D., Schiavon, R. P., et al. 2003, ApJ, 584, 76
Chabrier, G. 2003, PASP, 115, 763
Coil, A. L., Newman, J. A., Kaiser, N., et al. 2004, ApJ, 617, 765
Connolly, A. J., Szalay, A. S., Dickinson, M., Subbarao, M. U., & Brunner, R. J. 1997, ApJ, 486, L11
Cowie, L. L., Songaila, A., & Barger, A. J. 1999, AJ, 118, 603
Cowie, L. L., Songaila, A., Hu, E. M., & Cohen, J. G. 1996, AJ, 112, 839
da Cunha, E., Charlot, S., & Elbaz, D. 2008, MNRAS, 388, 1595
Daddi, E., Dickinson, M., Morrison, G., et al. 2007, ApJ, 670, 156
Davis, M., Guhathakurta, P., Konidaris, N. P., et al. 2007, ApJ, 660, L1
Devereux, N., Duric, N., & Scowen, P. A. 1997, AJ, 113, 236
Dickinson, M., & GOODS Legacy Team. 2001, BAAS, 33, 820
Doherty, M., Bunker, A., Sharp, R., et al. 2006, MNRAS, 370, 331
Donley, J. L., Rieke, G. H., Pérez-González, P. G., & Barro, G. 2008, ApJ, 687, 111
Dutton, A. A., van den Bosch, F. C., & Dekel, A. 2010, MNRAS, 405, 1690
Elbaz, D., Daddi, E., Le Borgne, D., et al. 2007, A&A, 468, 33
Erb, D. K., Steidel, C. C., Shapley, A. E., et al. 2006, ApJ, 647, 128
Faber, S. M., Willmer, C. N. A., Wolf, C., et al. 2007, ApJ, 665, 265
Fioc, M., & Rocca-Volmerange, B. 1997, A&A, 326, 950
Flores, H., Hammer, F., Elbaz, D., et al. 2004, A&A, 415, 885
Flores, H., Hammer, F., Thuan, T. X., et al. 1999, ApJ, 517, 148
Garn, T., Sobral, D., Best, P. N., et al. 2010, MNRAS, 402, 2017
Geach, J. E., Smail, I., Best, P. N., et al. 2008, MNRAS, 388, 1473
Gilbank, D. G., Bower, R. G., Glazebrook, K., et al. 2011, MNRAS, 414, 304
Glazebrook, K., Blake, C., Economou, F., Lilly, S., & Colless, M. 1999, MNRAS, 306, 843
Hammer, F., Flores, H., Elbaz, D., et al. 2005, A&A, 430, 115
Hayes, M., Schaerer, D., & Östlin, G. 2010, A&A, 509, L5
Hopkins, A. M., & Beacom, J. F. 2006, ApJ, 651, 142
Hopkins, A. M., Connolly, A. J., & Szalay, A. S. 2000, AJ, 120, 2843
Karim, A., Schinnerer, E., Martínez-Sansigre, A., et al. 2011, ApJ, 730, 61
Kauffmann, G., Heckman, T. M., White, S. D. M., et al. 2003, MNRAS, 341, 54
Kennicutt, R. C., Jr. 1998, ARA&A, 36, 189
Kennicutt, R. C., Hao, C., Calzetti, D., et al. 2009, ApJ, 703, 1672
Kroupa, P. 2001, MNRAS, 322, 231
Laird, E. S., Nandra, K., Georgakakis, A., et al. 2009, ApJS, 180, 102
Lee, J. C., Gil de Paz, A., Tremonti, C., et al. 2009, ApJ, 706, 599
Le Floc'h, E., Papovich, C., Dole, H., et al. 2005, ApJ, 632, 169
Leitherer, C., Ferguson, H. C., Heckman, T. M., & Lowenthal, J. D. 1995, ApJ, 454, L19
Lilly, S. J., Le Fevre, O., Hammer, F., & Crampton, D. 1996, ApJ, 460, L1
Ly, C., Lee, J. C., Dale, D. A., et al. 2011, ApJ, 726, 109
Maraston, C. 2005, MNRAS, 362, 799
Martin, D. C., Fanson, J., Schiminovich, D., et al. 2005, ApJ, 619, L1
Martin, D. C., Wyder, T. K., Schiminovich, D., et al. 2007, ApJS, 173, 342
Miyazaki, S., Hamana, T., Ellis, R. S., et al. 2007, ApJ, 669, 714
Noeske, K. G., Faber, S. M., Weiner, B. J., et al. 2007a, ApJ, 660, L47
Noeske, K. G., Weiner, B. J., Faber, S. M., et al. 2007b, ApJ, 660, L43
Oey, M. S., & Kennicutt, R. C., Jr. 1997, MNRAS, 291, 827
Park, S. Q., Barmby, P., Willner, S. P., et al. 2010, ApJ, 717, 1181
Pascual, S., Gallego, J., & Zamorano, J. 2007, PASP, 119, 30 (P07)
Pérez-González, P. G. 2003, PASP, 115, 1353
Pérez-González, P. G., Gil de Paz, A., Zamorano, J., et al. 2003, MNRAS, 338, 525 (PG03)
Pérez-González, P. G., Kennicutt, R. C., Jr., Gordon, K. D., et al. 2006, ApJ, 648, 987
Pérez-González, P. G., Rieke, G. H., Egami, E., et al. 2005, ApJ, 630, 82
Pérez-González, P. G., Rieke, G. H., Villar, V., et al. 2008, ApJ, 675, 234
Ranalli, P., Comastri, A., & Setti, G. 2003, A&A, 399, 39
Reddy, N. A., & Steidel, C. C. 2009, ApJ, 692, 778
Rieke, G. H., Alonso-Herrero, A., Weiner, B. J., et al. 2009, ApJ, 692, 556
Rodighiero, G., Cimatti, A., Gruppioni, C., et al. 2010, A&A, 518, L25
Salim, S., Dickinson, M., Michael Rich, R., et al. 2009, ApJ, 700, 161
Salim, S., Rich, R. M., Charlot, S., et al. 2007, ApJS, 173, 267
Salpeter, E. E. 1955, ApJ, 121, 161
Schiminovich, D., Ilbert, O., Arnouts, S., et al. 2005, ApJ, 619, L47
Sobral, D., Best, P. N., Geach, J. E., et al. 2009, MNRAS, 398, 75
Sobral, D., Best, P. N., Smail, I., et al. 2011, MNRAS, 411, 1675 (S11)
Stark, D. P., Ellis, R. S., Bunker, A., et al. 2009, ApJ, 697, 1493
Steidel, C. C., Adelberger, K. L., Giavalisco, M., Dickinson, M., & Pettini, M. 1999, ApJ, 519, 1
Steidel, C. C., Giavalisco, M., Pettini, M., Dickinson, M., & Adelberger, K. L. 1996, ApJ, 462, L17
Steidel, C. C., Shapley, A. E., Pettini, M., et al. 2004, ApJ, 604, 534
Stern, D., Eisenhardt, P., Gorjian, V., et al. 2005, ApJ, 631, 163
Strateva, I., Ivezić, Ž., Knapp, G. R., et al. 2001, AJ, 122, 1861
Tresse, L., Maddox, S. J., Le Fèvre, O., & Cuby, J.-G. 2002, MNRAS, 337, 369
Villar, V., Gallego, J., Pérez-González, P. G., et al. 2008, ApJ, 677, 169 (V08)
Willmer, C. N. A., Faber, S. M., Koo, D. C., et al. 2006, ApJ, 647, 853
Wilson, G., Cowie, L. L., Barger, A. J., & Burke, D. J. 2002, AJ, 124, 1258
Wright, E. L. 2006, PASP, 118, 1711
Wyder, T. K., Martin, D. C., Schiminovich, D., et al. 2007, ApJS, 173, 293
Yan, L., McCarthy, P. J., Freudling, W., et al. 1999, ApJ, 519, L47
Yoshikawa, T., Akiyama, M., Kajisawa, M., et al. 2010, ApJ, 718, 112
Zamorano, J., Gallego, J., Rego, M., Vitores, A. G., & Alonso, O. 1996, ApJS, 105, 343
Zamorano, J., Rego, M., Gallego, J. G., et al. 1994, ApJS, 95, 387